

Candidate Water Vapor Lines to Locate the H₂O Snowline through High-Dispersion Spectroscopic Observations II. The Case of a Herbig Ae Star

Shota Notsu^{1,8}, Hideko Nomura², Daiki Ishimoto^{1,2}, Catherine Walsh^{3,4}, Mitsuhiro Honda⁵, Tomoya Hirota⁶, and T. J. Millar⁷

¹*Department of Astronomy, Graduate School of Science, Kyoto University, Kitashirakawa-Oiwake-cho, Sakyo-ku, Kyoto 606-8502, Japan*

²*Department of Earth and Planetary Science, Tokyo Institute of Technology, 2-12-1 Ookayama, Meguro-ku, Tokyo 152-8551, Japan*

³*Leiden Observatory, Leiden University, P.O. Box 9513, 2300 RA Leiden, The Netherlands*

⁴*School of Physics and Astronomy, University of Leeds, Leeds, LS2 9JT, UK*

⁵*Department of Physics, School of Medicine, Kurume University, 67 Asahi-machi, Kurume, Fukuoka 830-0011, Japan*

⁶*National Astronomical Observatory of Japan, 2-21-1 Osawa, Mitaka, Tokyo 181-8588, Japan*

⁷*Astrophysics Research Centre, School of Mathematics and Physics, Queen's University Belfast, University Road, Belfast, BT7 1NN, UK*

⁸*Research Fellow of Japan Society for the Promotion of Science (DC1)*

snotsu@kusastro.kyoto-u.ac.jp

This paper was received by The Astrophysical Journal (ApJ) on October 27th, 2016, and was accepted on January 13th, 2017.

ABSTRACT

Observationally measuring the location of the H₂O snowline is crucial for understanding the planetesimal and planet formation processes, and the origin of water on Earth. In disks around Herbig Ae stars ($T_* \sim 10,000\text{K}$, $M_* \gtrsim 2.5M_\odot$), the position of the H₂O snowline is further from the central star compared with that around cooler, and less massive T Tauri stars. Thus, the H₂O emission line fluxes from the region within the H₂O snowline are expected to be stronger. In this paper, we calculate the chemical composition of a Herbig Ae disk using chemical kinetics. Next, we calculate the H₂O emission line profiles, and investigate the properties of candidate water lines across a wide range of wavelengths (from mid-infrared to sub-millimeter) that can locate the position of the H₂O snowline. Those line identified have small Einstein A coefficients ($\sim 10^{-6} - 10^{-3} \text{ s}^{-1}$) and relatively high upper state energies ($\sim 1000\text{K}$). The total fluxes tend to increase with decreasing wavelengths. We investigate the possibility of future observations (e.g., ALMA, SPICA/SMI-HRS) to locate the position of the H₂O snowline. Since the fluxes of those identified lines from Herbig Ae disks are stronger than those from T Tauri disks, the possibility of a successful detection is expected to increase for a Herbig Ae disk.

Subject headings: astrochemistry— protoplanetary disks— ISM: molecules— sub-millimeter & infrared: planetary systems— stars: formation

1. Introduction

Observationally locating the position of the H₂O snowline (Hayashi 1981; Hayashi et al. 1985) in a protoplanetary disk is important. It will provide information on the physical and chemical conditions in disks, such as the temperature structure, the dust-grain size distribution, and the water vapor distribution in the disk midplane (e.g., Oka et al. 2011; Piso et al. 2015), and will give constraints on the current formation theories of planetesimals and planets (e.g., Öberg et al. 2011; Okuzumi et al. 2012; Ros & Johansen 2013). It will help clarify the origin of water on rocky planets including the Earth (e.g., Morbidelli et al. 2000, 2012, 2016; Sato et al. 2016). Banzatti et al. (2015) and Cieza et al. (2016) recently showed that the presence of the H₂O snowline leads to a sharp discontinuity in the radial profile of the dust emission spectral index, due to the replenishment of small grains through fragmentation because of the change in fragmentation velocities across the H₂O snowline. Through recent space and ground infrared spectroscopic observations for protoplanetary disks, some infrared H₂O lines, which mainly trace the disk surface, have been detected (for more details, see e.g., Pontoppidan et al. 2010b; van Dishoeck et al. 2014; Blevins et al. 2016; Banzatti et al. 2016; Notsu et al. 2016).

The velocity profiles of emission lines from protoplanetary disks are usually affected by Doppler shift due to Keplerian rotation and thermal broadening. Therefore, the velocity profiles are sensitive to the radial distribution of the line-emitting regions. In our previous paper (paper I, Notsu et al. 2016), we calculated the chemical composition and the H₂O line profiles in a T Tauri disk¹, and identified candidate H₂O lines especially at sub-millimeter wavelengths, to locate the position of the H₂O snowline through future high-dispersion spectroscopic observations. Our calculations showed that the fluxes of H₂O lines with small Einstein A coefficients ($A_{ul} \sim 10^{-6} - 10^{-3} \text{ s}^{-1}$) and relatively high upper state energies ($E_{\text{up}} \sim 1000\text{K}$) are dominated by the disk region inside the H₂O snowline. Therefore, their profiles

¹In the remainder of this paper, we define the protoplanetary disks around T Tauri/Herbig Ae stars as “T Tauri/Herbig Ae disks”.

could be used to locate the position of the H₂O snowline. This is because the water gas column density of the region inside the H₂O snowline is high enough that all lines are optically thick as long as $A_{ul} > 10^{-6} \text{ s}^{-1}$. On the other hand, the region outside the H₂O snowline has lower water gas column densities and lines with larger Einstein A coefficients have a more significant contribution to their fluxes since the lines are optically thin. The wavelengths of those candidate lines we identified to locate the position of the H₂O snowline overlap with the capabilities of ALMA. In addition, we calculated the profiles of lines which have been detected by previous spectroscopic observations using *Herschel* (e.g., the ortho-H₂O 63.32 μm and 538.29 μm lines). These lines are less suited to locate the position of the H₂O snowline, because they are not dominated in flux by the region inside the snowline.

In this work (paper II), we extend our disk chemical model and the H₂O line profile calculations to the case of a Herbig Ae disk. We discuss the differences in disk chemical structures and line properties between the cases of a T Tauri disk (paper I) and a Herbig Ae disk (this paper). We investigate the line properties in detail for candidate water lines to locate the position of the H₂O snowline over a wide wavelength range from mid-infrared to sub-millimeter, and discuss the possibility of detecting such lines with future observations. The methods are outlined in Section 2. The results and discussions are described in Sections 3 and 4, respectively, and the conclusions are listed in Section 5.

2. Methods

The physical structures of the protoplanetary disk models used here are calculated using the methods in Nomura & Millar (2005) including X-ray heating (Nomura et al. 2007). A more detailed description of the background theory and computation of this physical model is described in the original papers (Nomura & Millar 2005; Nomura et al. 2007) and paper I (Notsu et al. 2016). Walsh et al. (2010, 2012, 2014a, 2015), Heinzeller et al. (2011), Furuya et al. (2013), Notsu et al. (2015), and Notsu et al. (2016) used the same physical models for a T Tauri disk and a Herbig

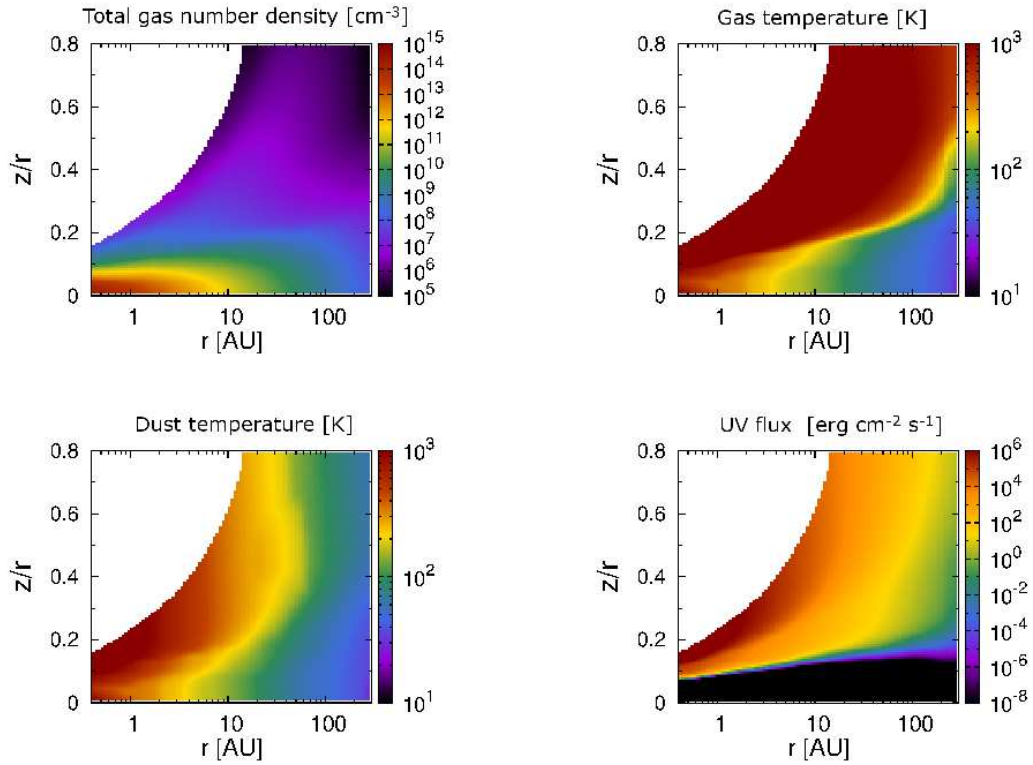


Fig. 1.— The total gas number density in cm^{-3} (top left), the gas temperature in Kelvin (top right), the dust temperature in Kelvin (bottom left), and the UV flux in $\text{erg cm}^{-2} \text{s}^{-1}$ (bottom right) of a Herbig Ae disk as a function of the disk radius in au and height (scaled by the radius, z/r) up to maximum radius of $r = 300$ au.

Ae disk to study various chemical and physical effects, and they also describe the calculation of the physical structures in detail.

In paper I (Notsu et al. 2016), we adopted the physical model of a steady, axisymmetric Keplerian disk surrounding a T Tauri star with mass $M_*=0.5M_\odot$, radius $R_*=2.0R_\odot$, and effective temperature $T_*=4000\text{K}$ (Kenyon & Hartmann 1995). In this paper, we adopt the physical model of a disk surrounding a Herbig Ae star with $M_*=2.5M_\odot$, $R_*=2.0R_\odot$, and $T_*=10,000\text{K}$ (see also Walsh et al. 2015). In our disk physical models, we adopt a viscous parameter $\alpha=10^{-2}$, a mass accretion rate $\dot{M}=10^{-8}M_\odot \text{ yr}^{-1}$, and gas-to-dust mass ratio $g/d = 100$. The values of total disk mass are $M_{\text{disk}} \sim 2.4 \times 10^{-2}M_\odot$ for the T Tauri disk (Heinzeller et al. 2011), and $M_{\text{disk}} \sim 2.5 \times 10^{-2}M_\odot$ for the Herbig Ae disk. We adopt the same compact and spherical dust-grain model of Nomura & Millar (2005). They assume that dust and gas are well mixed, and that the dust grains consist of silicate grains, carbonaceous grains, and water ices. They adopt the dust-grain size distribution which is consistent with the extinction curve observed in dense clouds (Mathis et al. 1977; Weingartner & Draine 2001). The stellar UV radiation field in our Herbig Ae disk model has no excess emission components (e.g., optically thin hydrogenic bremsstrahlung radiation and Lyman- α line emission), although that in our T Tauri disk model has such excess emission components (for more detail, see Nomura & Millar 2005, Walsh et al. 2015 and Notsu et al. 2016). In Figure 1, we display the gas number density in cm^{-3} (top left), the gas temperature in K (top right, T_g), the dust-grain temperature in K (bottom left, T_d), and the wavelength-integrated UV flux in $\text{erg cm}^{-2} \text{ s}^{-1}$ (bottom right) of a Herbig Ae disk as a function of disk radius in au and height (scaled by the radius, z/r).

Here we focus on the differences between the physical structures of the T Tauri disk (see Figure 1 of paper I, Notsu et al. 2016) and the Herbig Ae disk. The density in the atmosphere of the Herbig Ae disk (e.g., $n_{\text{H}} = 6 \times 10^{10} \text{ cm}^{-3}$ at $r = 5 \text{ au}$ and $z/r = 0.1$) is lower than that of the T Tauri disk (e.g., $n_{\text{H}} = 2 \times 10^{11} \text{ cm}^{-3}$ at $r = 5 \text{ au}$ and

$z/r = 0.1$), because the scale height² H of the Herbig Ae disk (e.g., $H/r \sim 1.2$ at $r = 5 \text{ au}$) is smaller than that for the disks around the T Tauri disk (e.g., $H/r \sim 1.7$ at $r = 5 \text{ au}$). The gas density and temperature distributions of the disks are obtained self-consistently by iteratively solving the equations for hydrostatic equilibrium in the vertical direction and local thermal balance between heating and cooling of gas (Nomura & Millar 2005). The gas and dust temperatures throughout most of the Herbig Ae disk, and the strength of the UV flux in the disk surface of the Herbig Ae disk are higher compared with those of the T Tauri disk, although the stellar UV radiation field in our Herbig Ae disk model has no excess emission components, apart from that in our T Tauri disk model. This is because the photospheric black-body radiative flux from the central Herbig Ae star is larger than that from the central T Tauri star. The strength of the X-ray flux in the disk surface of the Herbig Ae disk is lower compared with that of the T Tauri disk, since we adopted a smaller value of X-ray luminosity in the Herbig Ae disk ($L_X \sim 3 \times 10^{29} \text{ erg s}^{-1}$) compared with that in the T Tauri disk ($L_X \sim 10^{30} \text{ erg s}^{-1}$).

To investigate the chemical structure of the Herbig Ae disk, we use a large chemical network which includes gas-phase reactions and gas-grain interactions (freeze-out of gas molecules on dust grains, and thermal and non-thermal desorption from dust grains). The initial elemental fractional abundances (relative to total hydrogen nuclei density) we use are the set of atomic oxygen-rich low-metallicity abundances from Graedel et al. (1982), listed in Table 8 of Woodall et al. (2007), which is the same set as used in paper I (Notsu et al. 2016). We adopt the same chemical network as described in paper I (Notsu et al. 2016). Henning & Semenov (2013), Dutrey et al. (2014), and Haworth et al. (2016) reviewed the recent development of calculations for chemical structure in protoplanetary disks.

Using the H_2O gas abundance distribution obtained from our chemical calculation described in the previous paragraph, we calculate the H_2O emission line profiles ranging from near-infrared to sub-millimeter wavelengths from the Herbig

² $H = c_s/\Omega \propto M_*^{-0.5}T_g^{0.5}$, where c_s and Ω are the sound speed and Keplerian angular velocity, respectively.

Ae disk assuming Keplerian rotation, and identify the lines which are the best candidates for probing emission from the inner thermally desorbed water reservoir, i.e., within the H₂O snowline. We also study how the line fluxes and profile shapes depend on the position of the H₂O snowline. In paper I (Notsu et al. 2016), we adopted the same calculation method to determine the H₂O emission line profiles from a T Tauri disk (based on Rybicki & Lightman 1986, Hogerheijde & van der Tak 2000, Nomura & Millar 2005, and Schöier et al. 2005), with the detailed model explained in Section 2.3 of paper I. The code which we have built for calculating emission line profiles is a modification of the original 1D code called RATRAN³ (Hogerheijde & van der Tak 2000). We adopt the data of line parameters in the Leiden Atomic and Molecular Database LAMDA⁴ (Schöier et al. 2005). Here we note that in our method, we adopt the assumption of local thermal equilibrium (LTE) to obtain the level populations of the water molecule (n_u and n_l). In Section 4.2, we discuss the validity of this assumption. In addition, we set the ortho to para ratio (OPR) of water to its high-temperature value of 3 throughout the disk.

3. Results

3.1. The distributions of H₂O gas and ice

Figure 2 shows the fractional abundances (relative to total gas hydrogen nuclei density, n_{H}) of H₂O gas and ice in a Herbig Ae disk as a function of disk radius r and height scaled by the radius (z/r). Here we focus on the differences in H₂O distributions between the cases of a Herbig Ae disk and a T Tauri disk (see Figure 2 of paper I, Notsu et al. 2016).

The H₂O snowline of the Herbig Ae disk exists at a radius of $r \sim 14$ au in the midplane ($T_g \sim T_d \sim 120\text{K}$), which is significantly larger than that for the T Tauri disk model ($r \sim 1.6$ au, see Figure 2 of paper I, Notsu et al. 2016). This is because the gas and dust temperatures, which are coupled in the midplane of the Herbig

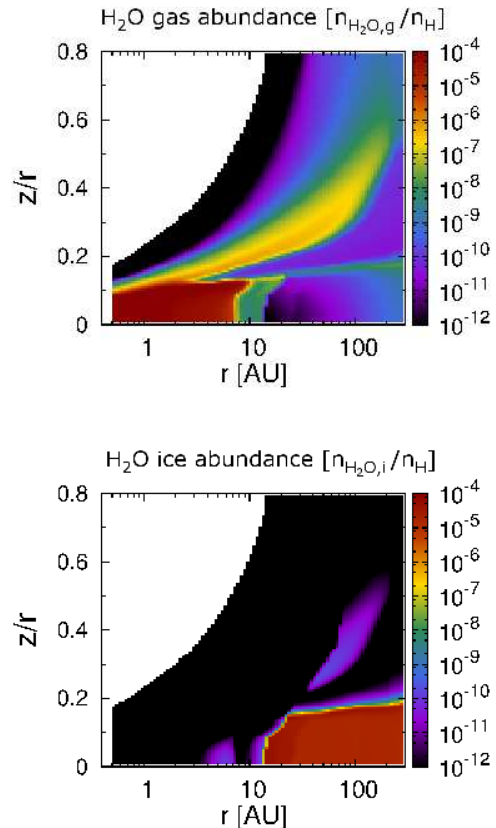


Fig. 2.— The fractional abundance (relative to total hydrogen nuclei density) distributions of H₂O gas (top) and H₂O ice (bottom) of a Herbig Ae disk as a function of disk radius and height (scaled by the radius, z/r) up to maximum radius of $r = 300\text{au}$.

³<http://home.strw.leidenuniv.nl/~michiel/ratran/>

⁴<http://home.strw.leidenuniv.nl/~moldata/>

Ae disk, are higher than that of our T Tauri disk. Inside the H₂O snowline, the temperature exceeds the sublimation temperature under the pressure conditions in the midplane of the Herbig Ae disk ($T_g \sim T_d \sim 120\text{K}$), and most of the H₂O is released into the gas-phase by thermal desorption. Here we note that the sublimation temperature under the pressure conditions in the midplane of the Herbig Ae disk ($T_g \sim T_d \sim 120\text{K}$) is lower than that in the midplane of the T Tauri disk ($T_g \sim T_d \sim 150 - 160\text{K}$, see paper I Notsu et al. 2016). The region in the midplane of the Herbig Ae disk where the temperature is around 100–200K is at a larger radius compared with that in the midplane of T Tauri disk, and the gas number density of such a region in the midplane of the Herbig Ae disk is lower ($n_{\text{H}} \sim 10^{11} - 10^{12} \text{ cm}^{-3}$) versus ($n_{\text{H}} \sim 10^{12} - 10^{13} \text{ cm}^{-3}$). According to Eq. (3)-(5) in Section 2.2.2 of paper I (Notsu et al. 2016), the sublimation temperature is higher if the gas number density is also higher.

The temperature of the region just inside the H₂O snowline in the Herbig Ae disk (between 7–8 au and 14 au) is $T_g \sim 120 - 170\text{K}$; hence the gas-phase chemistry to form H₂O molecules (e.g., $\text{O} + \text{H}_2 \rightarrow \text{OH} + \text{H}$ and $\text{OH} + \text{H}_2 \rightarrow \text{H}_2\text{O} + \text{H}$) is not efficient compared with the inner region at a higher temperature ($T_g > 170\text{K}$, $r < 7 - 8\text{au}$). We point out that the radial temperature profile in the midplane of the T Tauri disk is steeper than that in the midplane of the Herbig Ae disk, and this is another reason why the T Tauri disk does not have such a region with a relatively large fractional abundance of H₂O gas ($\sim 10^{-8}$). A similar distribution of gas-phase H₂O in the midplane of a Herbig Ae disk is reported in Figure 1 of Woitke et al. (2009b). Here we also note that Eistrup et al. (2016) calculated the chemical evolution of a disk midplane under both molecular and atomic initial conditions as initial chemical abundances. They showed that in the latter atomic conditions, the abundance of H₂O gas and ice around the H₂O snowline ($\sim 10^{-6}$) is smaller than that for molecular initial abundances ($\sim 10^{-4}$). This is because O₂ is formed in the gas-phase via $\text{O} + \text{OH} \rightarrow \text{O}_2 + \text{H}$ and remains in the gas phase since its sublimation temperature is much lower than that of other molecules like H₂O. This reaction route competes with gas-phase H₂O formation.

In the outer disk, the fractional abundance of H₂O gas is also relatively high ($\sim 10^{-8} - 10^{-7}$) in the hot surface layer and at the H₂O sublimation (photodesorption) front compared with the cold midplane region of the outer disk ($\lesssim 10^{-12} - 10^{-10}$), as also shown in the T Tauri disk model (paper I, Notsu et al. 2016).

Here we note that the region with a high H₂O gas abundance ($\sim 10^{-4}$) in the disk midplane extends to a larger radius ($r \sim 10$ au) at $z/r \gtrsim 0.1$ than at $z/r \sim 0$ ($r \sim 7 - 8$ au). This is not seen in the T Tauri disk case (see Figure 2 of paper I, Notsu et al. 2016). This is because the scale height of the Herbig Ae disk (e.g., $H/r \sim 1.2$ at $r = 5$ au) is smaller than that for the T Tauri disk (e.g., $H/r \sim 1.7$ at $r = 5$ au) and the radiation from the central Herbig Ae star is stronger than that from the central T Tauri star, thus the gas temperature of the Herbig Ae disk around $z/r \sim 0.1$ is higher. In contrast, for the T Tauri disk case, since the disk scale height is larger than that of Herbig Ae disk, the values of gas temperature of the disk between $z/r \sim 0 - 0.1$ is constant.

The top panel of Figure 3 shows the radial column density profiles of H₂O gas and ice for both the T Tauri disk (see Figure 3 of paper I, Notsu et al. 2016) and the Herbig Ae disk. In the Herbig Ae disk case, the column density of H₂O gas and ice in the disk midplane flips across the H₂O snowline as expected ($r \sim 14$ au). The column density of H₂O gas is high ($\sim 10^{20} - 10^{22} \text{ cm}^{-2}$) in the inner high-temperature region of the disk midplane with $r < 7 - 8$ au, relatively high ($\sim 10^{16} - 10^{19} \text{ cm}^{-2}$) in the midplane between 7–8 au and 14 au, and in contrast, low outside the H₂O snowline ($< 10^{16} \text{ cm}^{-2}$). The column density profile of H₂O ice is roughly opposite. In the T Tauri disk case, the column densities of H₂O gas and ice in the disk midplane flips across the H₂O snowline more steeply following the steeper temperature gradient. The Bottom panel of Figure 3 shows the radial profiles of the column density in cm^{-2} of H₂O ice and gas in the Herbig Ae disk, which have been vertically integrated from $z = \infty$ to (i) $-\infty$, (ii) $z(\tau_{17.75\mu\text{m}} = 1)$, (iii) $z(\tau_{61.32\mu\text{m}} = 1)$, and (iv) $z(\tau_{682.66\mu\text{m}} = 1)$. τ_λ is the total optical depth value at each wavelength, λ , including gas

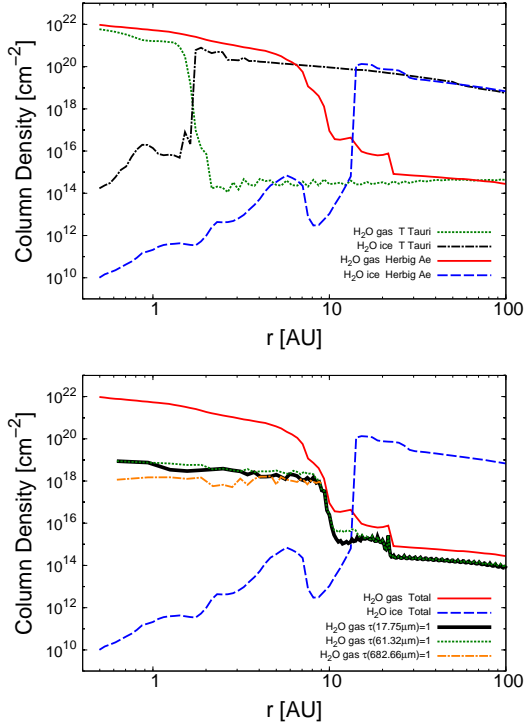


Fig. 3.— Top panel: The radial profiles of the vertically integrated column density in cm^{-2} of H_2O gas and ice in the T Tauri disk (*green dotted line* and *black dashed dotted line*) and the Herbig Ae disk (*red solid line* and *blue dashed line*). Bottom panel: The radial profiles of the column density in cm^{-2} of H_2O ice (*blue dashed line*) and gas in the Herbig Ae disk, which are vertically integrated from $z = \infty$ to $-\infty$ (*red solid line*), to $z(\tau_{17.75\mu\text{m}} = 1)$ (*black bold solid line*), to $z(\tau_{61.32\mu\text{m}} = 1)$ (*green dotted line*), and to $z(\tau_{682.66\mu\text{m}} = 1)$ (*orange dashed dotted line*). Since $\tau_{682.66\mu\text{m}}$ at $z = -\infty$ is lower than unity at $r \gtrsim 10$ au, the radial profile of this case is plotted only $r \lesssim 10$ au.

and dust components. In Section 4.3, we discuss about this panel in detail.

Previous analytical models and numerical simulations derived the position of the H_2O snowline of an optically thick disk for given parameters, such as mass (M_*) and temperature (T_*) of the central star, a viscous parameter α , an accretion rate \dot{M} , a gas-to-dust mass ratio g/d , and the average dust grain size a and opacity (e.g., Davis 2005; Garaud & Lin 2007; Min et al. 2011; Oka et al. 2011; Du & Bergin 2014; Harsono et al. 2015; Mulders et al. 2015; Piso et al. 2015; Sato et al. 2016), and suggested that the position of the H_2O snowline changes, as these parameters change. In the case of Herbig Ae disks with $M_* \sim 2.5M_\odot$, $\dot{M} \sim 10^{-8}M_\odot \text{ yr}^{-1}$, $g/d = 100$, and $a \sim 0.1\mu\text{m}$, the position of the H_2O snowline is $\sim 10 - 20$ au. In our calculations we use similar parameters for M_* , \dot{M} and a , and the H_2O snowline appears at a radius of around 14 au in the midplane, within the range of previous studies.

3.2. H_2O emission lines from a Herbig Ae disk

In this Section, we first describe the detailed properties of seven characteristic pure rotational ortho- H_2O lines (see Table 1 and Section 3.2.1) for the Herbig Ae disk. These seven lines (including the ortho- H_2O 682.66 μm line) are candidates for tracing emission from the hot water reservoir within the H_2O snowline. In Section 3.2.2, we describe the properties of the 63.32 and 538.29 μm lines, which are examples of lines which are less suited to trace emission from the water reservoir within the H_2O snowline. We consider these two lines to test the validity of our model calculations, since the fluxes of these two lines from protoplanetary disks have been observed with *Herschel*. The properties of near-, and mid-infrared H_2O emission lines which do not trace emission from the hot water vapor within the H_2O snowline are also described in this subsection. Since we investigated the profiles and properties of three lines ($\lambda=682.66, 63.32, 538.29\mu\text{m}$) for the T Tauri disk in paper I (Notsu et al. 2016), here we mainly focus on the differences between the line properties between the T Tauri disk and the Herbig Ae disk. In Section 3.2.3 and Section 4.4, we show and dis-

Discuss other candidate lines which trace the emission from the hot water vapor within the H₂O snowline from mid-infrared to sub-millimeter wavelengths, and their properties, especially the variation in line fluxes with wavelength. In Section 3.2.4, we show and discuss normalized radial cumulative line fluxes for the lines discussed in Sections 3.2.1-3.2.3.

In this paper, we show and discuss only the results concerning ortho-H₂O lines, since the number densities and the fluxes of ortho-H₂O lines are larger than those of para-H₂O lines, due to the assumption, OPR=3. The line selection process is described in detail in Section 3.2 of paper I (Notsu et al. 2016).

3.2.1. Candidate H₂O emission lines which trace emission from the hot water vapor within the H₂O snowline

Figure 4 shows the emission profiles of seven representative characteristic pure rotational ortho-H₂O lines at $\lambda=17.75\mu\text{m}$ (top left), $24.00\mu\text{m}$ (top center), $61.32\mu\text{m}$ (top right), $94.17\mu\text{m}$ (middle left), $482.99\mu\text{m}$ (middle center), $682.66\mu\text{m}$ (middle right), and $933.28\mu\text{m}$ (bottom), for the Herbig Ae disk. These lines have small values of A_{ul} ($\sim 10^{-3} - 10^{-6} \text{ s}^{-1}$) and relatively large values of upper E_{up} ($\sim 700 - 1900\text{K}$). They are representative candidate ortho-H₂O lines which trace emission from the hot water gas within the H₂O snowline. The H₂O $933.28\mu\text{m}$, $682.66\mu\text{m}$, and $482.99\mu\text{m}$ lines fall in ALMA band 7, 8, and 9, respectively. The H₂O $17.75\mu\text{m}$ line and $24.00\mu\text{m}$ line are Q band lines at mid-infrared wavelengths, and the H₂O $17.75\mu\text{m}$ line falls in the wavelength coverage of SPICA/SMI-HRS (see Section 4.4). The detailed parameters, such as transitions ($J_{K_a K_c}$), wavelength λ , frequency, A_{ul} , E_{up} , critical density $n_{\text{cr}} = A_{ul}/\langle\sigma v\rangle^5$, and total line fluxes are listed in Table 1. In Table 1, we also show the values of the total fluxes from both the Herbig Ae disk and the T Tauri disk (see also paper I, Notsu et al. 2016). In calculating the values from the T Tauri disk, we use the same method as

in paper I (Notsu et al. 2016). In calculating all line profiles in this paper (see Figures 4, 7, 10, and 14), we assume that the distance d to the object is 140pc (\sim the distance of Taurus molecular cloud), and the inclination angle i of the disk is 30 degs.

As shown in all panels in Figure 4, the contributions from the optically thin surface layer of the outer disk ($r = 14\text{-}30$ au) are very small compared with those from the optically thick region near the midplane of the inner disk ($r < 14$ au), and they show the characteristic double-peaked profile due to Keplerian rotation. This is because these lines, which have small Einstein A coefficients ($A_{ul} \sim 10^{-3} - 10^{-6} \text{ s}^{-1}$) and relatively large upper state energies ($E_{\text{up}} \sim 1000\text{K}$), mainly trace the hot H₂O vapor inside the H₂O snowline. In Section 2.3 and 3.2.1 of paper I (Notsu et al. 2016), we explained the reason why these lines have such properties.

In the cases of candidate H₂O lines except the $482.99\mu\text{m}$ and $682.66\mu\text{m}$ lines (see Figure 4), almost all of the emission fluxes ($> 95\%$) come from the region with a high H₂O gas abundance ($\sim 10^{-4}$, $r < 8$ au), and the position of the two peaks and the rapid drop in flux density between the peaks contains information on the position of the outer edge of this region. In contrast, in the cases of the $482.99\mu\text{m}$ and $682.66\mu\text{m}$ lines (see Figure 4), most of the emission fluxes ($\sim 80\text{-}90\%$) are emitted from the region with a high H₂O gas abundance ($\sim 10^{-4}$, $r < 8$ au), and some fluxes ($\sim 10\text{-}20\%$) are emitted from the region with a relatively high H₂O gas abundance ($\sim 10^{-8}$, $r = 8\text{-}14$ au). The position of the two peaks and the rapid drop in flux density between the peaks contains information on the distribution of hot H₂O gas within the H₂O snowline.

Figures 5 and 6 show the line-of-sight emissivity (emissivity times extinction, $\eta_{ul}e^{-\tau_{ul}}$; see Equation (14) of Paper I, Notsu et al. 2016) and the total optical depth, τ_{ul} (gas emission and dust) distributions of these seven H₂O lines, respectively. We assume that the inclination angle, i , of the disk is 0 deg in making these figures (see Figures 5, 6, 8, 9, and 13), and thus the line-of-sight direction is from $z = +\infty$ to $-\infty$ at each disk radius. In the left panels of Figure 5, we over-

⁵ $\langle\sigma v\rangle$ is the collisional rates for the excitation of H₂O by H₂ and electrons for an adopted collisional temperature of 200K from Faure & Josselin (2008).

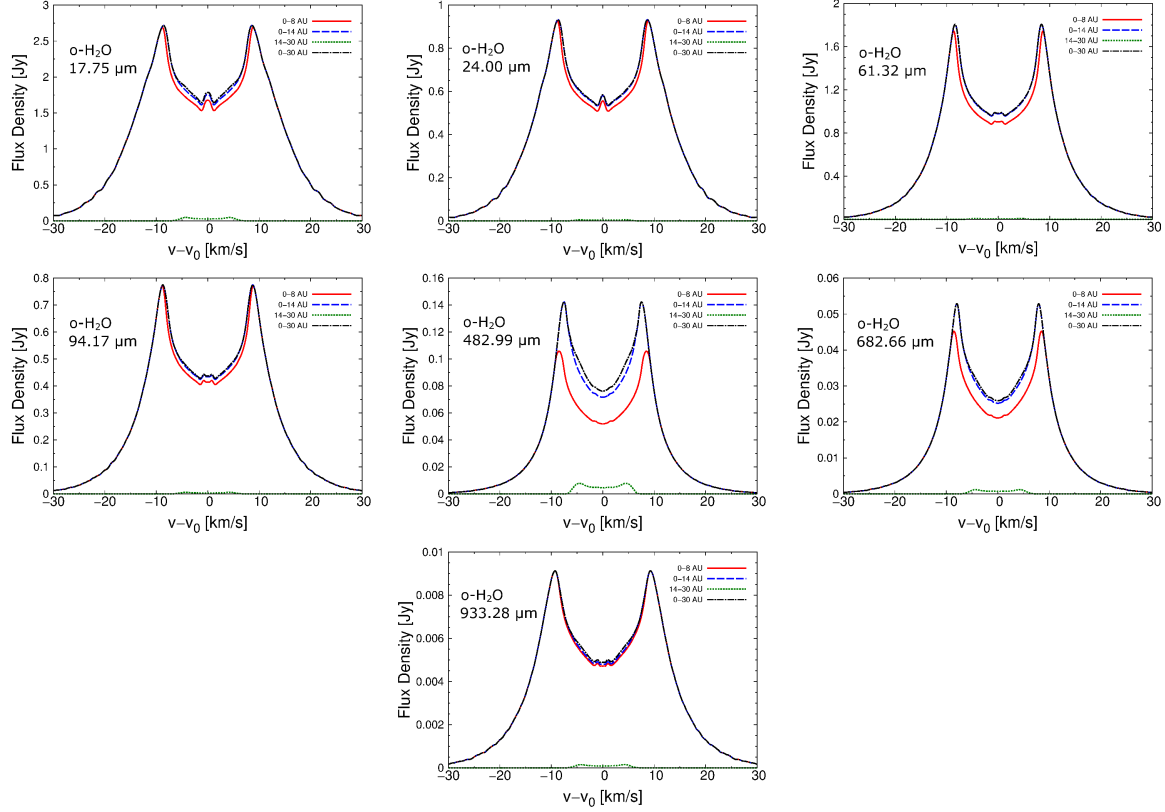


Fig. 4.— The velocity profiles of seven characteristic pure rotational ortho-H₂O lines at $\lambda=17.75\mu\text{m}$ (top left), $24.00\mu\text{m}$ (top center), $61.32\mu\text{m}$ (top right), $94.17\mu\text{m}$ (middle left), $482.99\mu\text{m}$ (middle center), $682.66\mu\text{m}$ (middle right), and $933.28\mu\text{m}$ (bottom), which have small A_{ul} and large E_{up} , from the Herbig Ae disk. These are candidate H₂O lines to trace the hot water vapor within the H₂O snowline. In calculating the line profiles in this paper (see Figures 4, 7, 10, and 14), we assume that the distance to the object d is 140pc (\sim the distance of Taurus molecular cloud), and the inclination angle of the disk, i , is 30 degree. The parameters and total fluxes of these H₂O lines are listed in Table 1 and B.1. *Red solid lines* are the emission line profiles from inside 8 au (=the inner high temperature region), *blue dashed lines* are those from inside 14 au (\sim inside the H₂O snowline), *green dotted lines* are those from 14-30 au (\sim outside the H₂O snowline), and *black dashed dotted lines* are those from the total area inside 30 au.

Table 1: Calculated representative ortho-H₂O line parameters and total line fluxes

$J_{K_a K_c}$	λ^1	Freq.	A_{ul}	E_{up}	n_{cr}	HAe flux ^{2,3}	TT flux ^{3,4}
	[μm]	[GHz]	[s^{-1}]	[K]	[cm^{-3}]	[W m^{-2}]	[W m^{-2}]
6 ₅₂ -5 ₀₅	17.754	16885.840	2.909×10^{-3}	1278.5	8.3×10^{10}	4.1×10^{-17}	2.3×10^{-20}
5 ₅₀ -5 ₀₅	23.996	12493.205	2.696×10^{-4}	1067.7	1.9×10^9	9.4×10^{-18}	6.4×10^{-21}
5 ₄₁ -6 ₁₆	61.316	4889.280	2.686×10^{-4}	878.1	4.1×10^8	5.9×10^{-18}	3.5×10^{-20}
6 ₅₂ -7 ₂₅	94.172	3183.464	3.387×10^{-4}	1278.5	3.1×10^8	1.8×10^{-18}	1.6×10^{-20}
5 ₃₂ -4 ₄₁	482.990	620.701	1.106×10^{-4}	732.1	3.3×10^6	5.3×10^{-20}	1.1×10^{-21}
6 ₄₃ -5 ₅₀	682.664	439.151	2.816×10^{-5}	1088.7	1.0×10^6	1.4×10^{-20}	3.1×10^{-22}
10 ₂₉ -9 ₃₆	933.277	321.226	6.165×10^{-6}	1861.2	4.7×10^6	2.3×10^{-21}	7.8×10^{-23}
8 ₁₈ -7 ₀₇	63.324	4734.296	1.772	1070.6	1.5×10^{10}	1.1×10^{-16}	5.7×10^{-18}
1 ₁₀ -1 ₀₁	538.289	556.936	3.497×10^{-3}	61.0	2.9×10^7	7.2×10^{-20}	1.1×10^{-20}
17 ₄₁₃ -16 ₃₁₄	12.396	24184.126	7.728	5780.8	1.1×10^{11}	6.7×10^{-17}	5.3×10^{-19}
13 ₇₆ -12 ₄₉	12.453	24073.032	1.053	4212.6	1.1×10^{13}	6.9×10^{-17}	2.5×10^{-19}
7 ₆₁ -6 ₅₂	4.958	60463.186	3.260	4180.4	1.6×10^{13}	2.2×10^{-16}	1.1×10^{-18}
7 ₆₁ -6 ₃₄	4.432	67646.817	2.080×10^{-4}	4180.4	6.5×10^{11}	5.0×10^{-20}	8.1×10^{-23}

¹ In calculating the value of line wavelength from the value of line frequency, we use the value of speed of light $c=2.99792458 \times 10^8 \text{ m s}^{-1}$.

² The total flux of each emission line from the Herbig Ae disk.

³ In calculating the total fluxes of these H₂O lines, we use a distance of $d = 140\text{pc}$ and an inclination angle of $i = 30$ degree.

⁴ The total flux of each emission line from the T Tauri disk (see also paper I, Notsu et al. 2016).

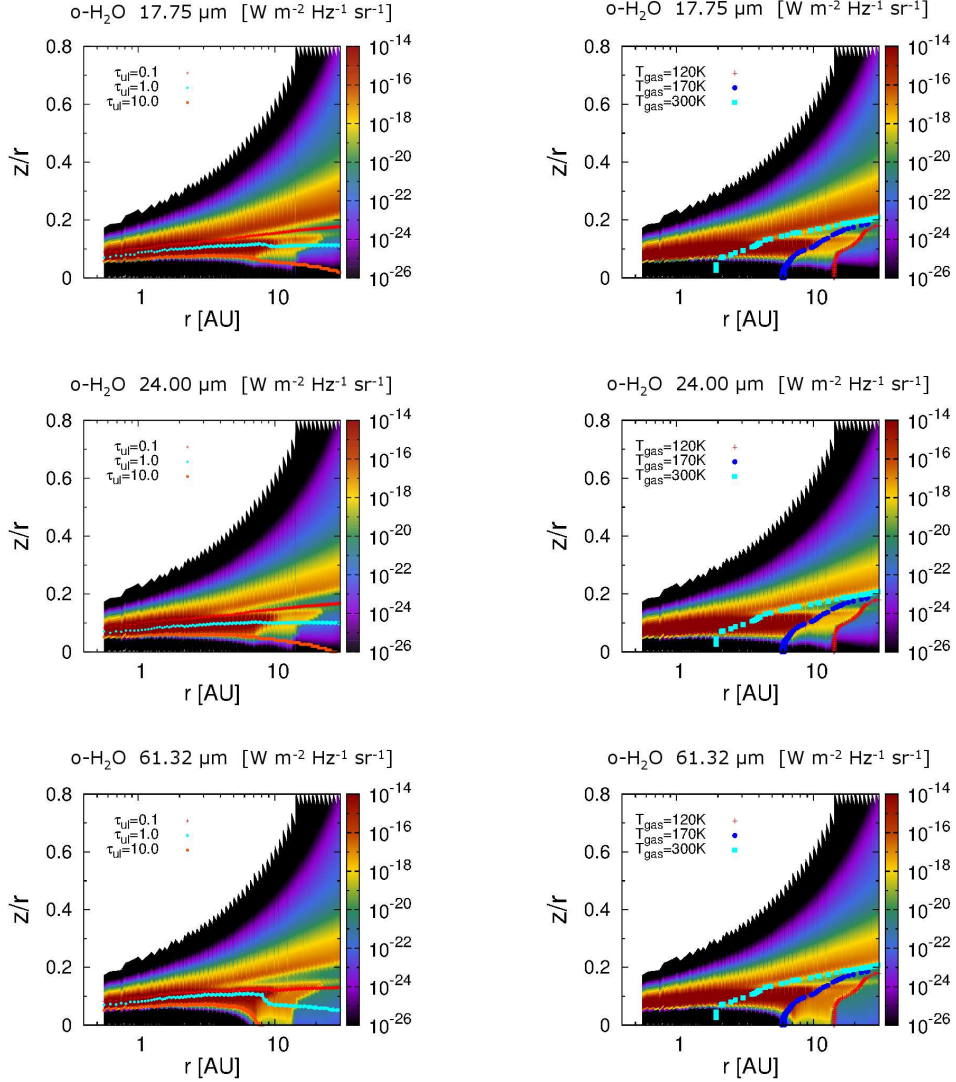


Fig. 5.— The line-of-sight emissivity distributions of the H₂O lines at $\lambda=17.75\mu m$ (top left and right), $24.00\mu m$ (middle left and right), $61.32\mu m$ (bottom left and right), which have small A_{ul} and large E_{up} , from the Herbig Ae disk. In the left panels, we overplot the total optical depth contours ($\tau_{ul} = 0.1$ (red cross points), 1 (cyan circle points), and 10 (orange square points)) on top of these line emissivity panels (see also Figure 6). In the right panels, we overplot the gas temperature T_g contours ($T_g = 120K$ (red cross points), 170K (blue circle points), and 300K (cyan square points), see also Figure 1). We assume that the inclination angle, i , of the disk is 0 deg in making these figures in this paper (see Figures 5, and 8), and the emissivity is calculated along the line from $z=+\infty$ to $-\infty$ at each disk radius. The units are $W m^{-2} Hz^{-1} sr^{-1}$.

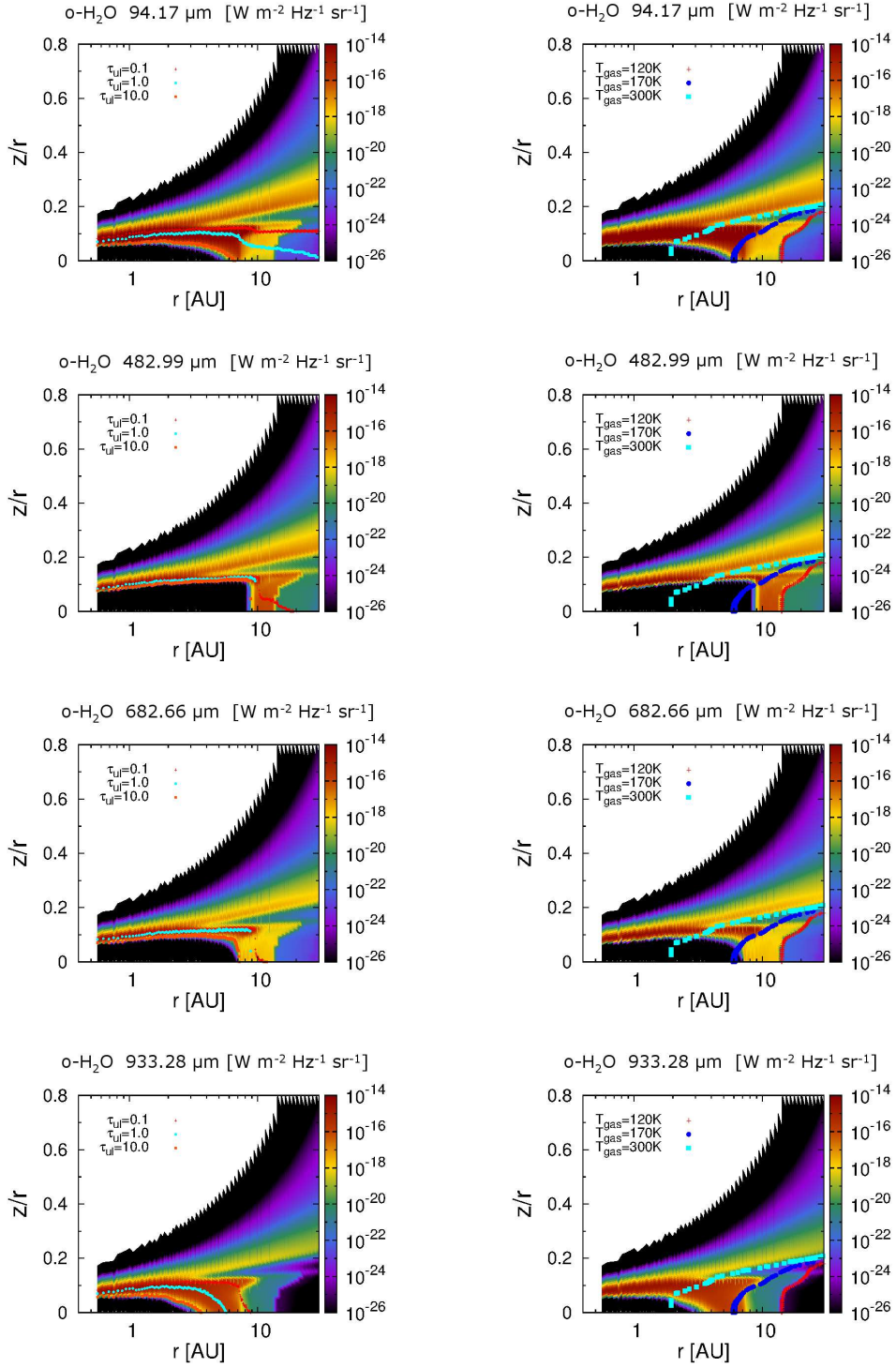


Fig. 5.— (Continued.) The line-of-sight emissivity distributions of the H₂O lines at $\lambda=94.17\mu\text{m}$ (top left and right), $482.99\mu\text{m}$ (second line left and right), $682.66\mu\text{m}$ (third line left and right), and $933.28\mu\text{m}$ (bottom left and right), which have small A_{ul} and large E_{up} , from the Herbig Ae disk.

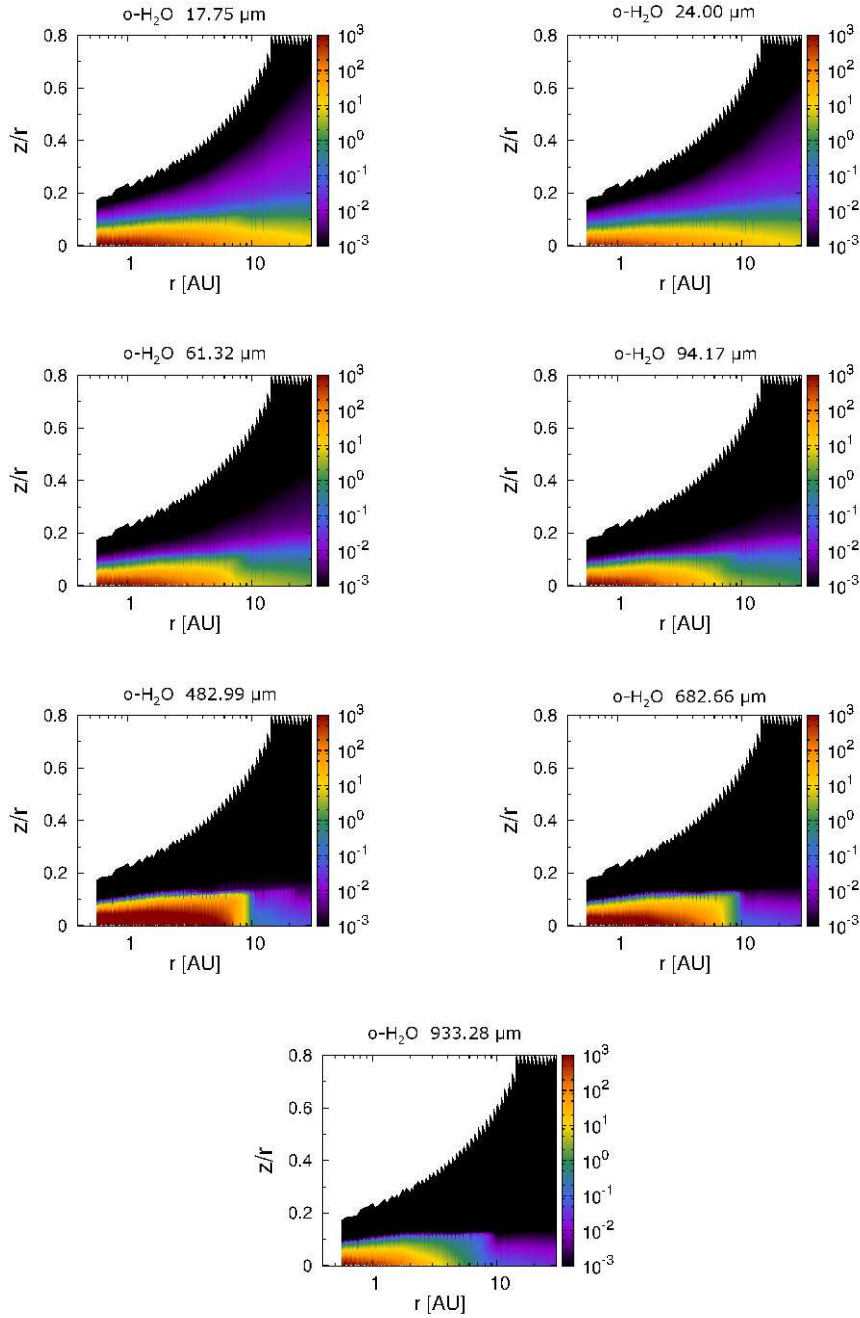


Fig. 6.— The line-of-sight total optical depth $\tau_{ul}(s, x, y, \nu)$ (gas emission and dust) distributions of the H_2O lines at $\lambda=17.75\mu\text{m}$ (top left), $24.00\mu\text{m}$ (top center), $61.32\mu\text{m}$ (top right), $94.17\mu\text{m}$ (middle left), $482.99\mu\text{m}$ (middle center), $682.66\mu\text{m}$ (middle right), and $933.28\mu\text{m}$ (bottom), which have small A_{ul} and large E_{up} , from the Herbig Ae disk. We assume that the inclination angle, i , of the disk is 0 deg in making these figures in this paper (see Figure 6 and 9), and thus the optical depth is calculated along the line from $z=+\infty$ to $-\infty$ at each disk radius. In calculating the values of $\tau_{ul}(s, x, y, \nu)$, we consider the contributions of both absorption by dust grains and the line absorption by the H_2O gas.

plot the total optical depth contours ($\tau_{ul}=0.1, 1,$ and 10) on top of these line emissivity panels (see also Figure 6). In the right panels, we overplot the gas temperature T_g contours ($T_g=120, 170,$ and 300K , see also Figure 1). Figure 13 in Appendix A shows the vertical distributions of the normalized cumulative line emissivity at $r=5$ au (top two panels), $r=10$ au (middle two panels), and $r=30$ au (bottom two panels), and of the gas temperature T_g . The left three panels show the distributions for these seven H_2O lines. We normalize the cumulative emissivity of each line using the values at $z=-\infty$. According to Figures 5, 6, and 13, the values of emissivity at $r \lesssim 14$ au (= the position of the H_2O snowline), $T_g \gtrsim 120\text{K}$, and $z/r \sim 0.05 - 0.12$ are larger than those of the optically thin hot surface layer and the photodesorbed layer of the outer disk, and in particular those in the region with a higher H_2O gas abundance ($\sim 10^{-4}$, $r < 7 - 8$ au, and $T_g \gtrsim 170\text{K}$) and $z/r \sim 0.05 - 0.12$ are much larger. Emission from $z \sim 0$ at $r \lesssim 7$ au is not possible to detect, because the optical depth of the inner disk midplane is high due to absorption by dust grains and excited H_2O molecules in the upper disk layer. Nevertheless, we can extract information on the distribution of hot H_2O vapor inside the H_2O snowline. This is because within $r < 14$ au (= the position of the H_2O snowline), the H_2O gas fractional abundance is relatively constant over $z/r \sim 0-0.1$ for the same disk radius r (see also Figure 2). Strictly speaking, as we described in Section 3.1, the region with a high H_2O gas abundance ($\sim 10^{-4}$) extends to a radius of $r \sim 10$ au at $z/r \sim 0.1$ compared with that at $z \sim 0$ ($r \sim 7-8$ au), and is reflected in the emissivity distribution. However, since the radial shift in the distribution is small (a few au), its influence is not so serious for obtaining information on the general trend of the H_2O distribution in the inner disk within the H_2O snowline.

The differences in the properties of the line profiles (see Figures 4, 5, 6, and 13) come from the differences in A_{ul} , E_{up} , and wavelengths among lines. For the lines with similar wavelengths, the values of optical depth tend to be larger as values of A_{ul} of the lines become larger, since the absorption by excited H_2O molecules increases. In addition, the values of optical depth become larger as values of E_{up} become smaller, since the line absorption be-

come stronger even in the colder region of the disk.

For the lines at shorter wavelengths, the opacity of the dust grains becomes larger (e.g., Nomura & Millar 2005). In the cases of shorter wavelength (mid- and far-infrared) lines, the absorption by the dust grains mainly determines total optical depth profiles (including gas and dust components) and line emitting regions in the both inner and outer disk. In contrast, for the lines with longer wavelengths, the values of the line absorption by excited molecules become larger (see also Equation (10) of Paper I (Notsu et al. 2016)) even if the values of A_{ul} and E_{up} are similar. In the case of longer wavelength lines (sub-millimeter lines), the line absorption by excited molecules mainly determines the total optical depth profiles and line emitting regions in the inner disk midplane with a high H_2O gas abundance ($\sim 10^{-4}$, $r < 7 - 8$ au), although the absorption by dust grains mainly determines those in the disk surface and outer colder disk midplane.

The H_2O $482.99\mu\text{m}$ and $682.66\mu\text{m}$ lines have relatively smaller values of E_{up} ($< 1100\text{K}$), and thus they can also trace outer colder region compared to lines with larger values of E_{up} . In addition, they have longer wavelengths ($> 400\mu\text{m}$) compared with other lines, thus the dust opacity is smaller and they can trace the regions closer to the midplane in the outer disk. These are the reasons why emission fluxes from the region with a relatively high H_2O gas abundance ($\sim 10^{-8}$, $r=8-14$ au) are not so small ($\sim 10 - 20\%$ of total emission fluxes) compared to the region with a high H_2O gas abundance ($\sim 10^{-4}$, $r < 8$ au). Although the H_2O $933.28\mu\text{m}$ line resides in the sub-millimeter region, this line has a larger E_{up} ($=1861.2\text{K}$) than other lines, and thus most of the emission flux is emitted from the region with high temperature and a high H_2O gas abundance ($\sim 10^{-4}$, $r < 8$ au).

Since the radial difference of the positions between the exact H_2O snowline location and the outer edge of the hot H_2O gas region is not so large (several au), the influence is not so serious when we want to get information on the overall H_2O distribution of the inner disk and roughly estimate the position of the H_2O snowline. However, if we observe several candidate H_2O lines

with small A_{ul} ($\sim 10^{-6} - 10^{-3}$), various E_{up} (e.g., $\sim 700 - 2100\text{K}$), and at various wavelengths between mid-infrared and sub-millimeter, there is the possibility to confine the detailed distribution, not only the position of the H_2O snowline, but also the H_2O gas abundance and the gas temperature in the disk midplane. In addition, we could trace the water reservoir within the H_2O snowline from the Keplerian line profiles independently regardless of the assumption of the relation between disk gas temperature and radius, as adopted in previous works to get the H_2O distributions (e.g., Zhang et al. 2013; Blevins et al. 2016). We note that the previous observations of H_2O lines with large A_{ul} ($\sim 10^{-1} - 10^0 \text{ s}^{-1}$) and very high E_{up} ($>3000\text{K}$) in many cases mainly trace the emission from the disk surface (e.g., Salyk et al. 2008; Pontoppidan et al. 2010a,b; Fedele et al. 2011; Mandell et al. 2012; van Dishoeck et al. 2014; Banzatti et al. 2016; Blevins et al. 2016, see also Section 3.2.2).

3.2.2. H_2O lines which are less suited to trace emission from water reservoir within the H_2O snowline

In the top left panel of Figure 7, we show the line profile for the H_2O $63.32\mu\text{m}$ line. The contribution from the optically thin surface layer of the outer disk ($r = 14\text{-}30 \text{ au}$) is large (three times larger in flux density) compared with that of the optically thick region near the midplane of inner disk ($r < 14 \text{ au}$), and the shape of the line profile is narrower by around a factor of two compared to those of candidate H_2O lines which trace the emission from the hot water vapor within the H_2O snowline. This is because the H_2O $63.32\mu\text{m}$ line has a large A_{ul} ($=1.772 \text{ s}^{-1}$), although E_{up} ($=1070.6\text{K}$) is similar to that of the candidate ortho- H_2O lines (e.g., $E_{up} = 1088.7\text{K}$ for the $682.66\mu\text{m}$ line). The detailed parameters, such as transitions ($J_{K_a K_c}$), wavelength, frequency, A_{ul} , E_{up} , critical density n_{cr} , and total line fluxes of the ortho- H_2O lines discussed in this subsection are listed in Table 1.

According to Figures 8, 9 and 13, the values of emissivity of the H_2O $63.32\mu\text{m}$ line in the optically thin hot surface layer of outer disk are as strong as that of the optically thick region inside the H_2O snowline. The area of the outer H_2O line

emitting region is larger than that of the inner region for this line, and thus emission from the outer part dominates. Therefore, we propose that this line is not optimal to detect emission from the hot water vapor within the H_2O snowline in Herbig Ae disk case, as we also found for the T Tauri disk (Notsu et al. 2016).

We note that previous space far-infrared low-dispersion spectroscopic observations with *Herschel*/PACS ($R \sim 1500$) detected some far-infrared H_2O emission lines with large A_{ul} ($\sim 10^{-1} - 10^0 \text{ s}^{-1}$) and relatively large E_{up} ($\sim 1000\text{K}$) including this $63.32\mu\text{m}$ line from the gas-rich Herbig Ae disk around HD163296, although the detections of these lines are only slightly above 3σ (e.g., Fedele et al. 2012, 2013; Meeus et al. 2012; Tilling et al. 2012; Dent et al. 2013). Although the profiles of these lines are spectrally unresolved, a comparison of line strength with models indicates that the emitting region of these observations originates in the hot surface layer of the outer disk ($r > 15 \text{ au}$, e.g., Fedele et al. 2012, 2013). The total integrated line flux of this H_2O $63.32\mu\text{m}$ line from the disk around HD163296 (at a distance d of $\sim 122 \text{ pc}$ and inclination i of 44 deg) is observed to be $(2.0 \pm 0.6) \times 10^{-17} \text{ W m}^{-2}$, and the values of the other lines (e.g., ortho- H_2O $56.82\mu\text{m}$ and $71.95\mu\text{m}$ lines) are roughly similar (e.g., Fedele et al. 2012; Meeus et al. 2012). Meeus et al. (2012) and Fedele et al. (2013) determined that the upper limits of the total fluxes of such H_2O emission lines, including the H_2O $63.32\mu\text{m}$ from other Herbig Ae disks ($d \sim 100 - 150 \text{ pc}$), are between a few 10^{-18} and a few $10^{-17} \text{ W m}^{-2}$. These values are roughly several tens of times smaller than the value which we calculate in this paper for this particular Herbig Ae disk model (see also Table 1, $d = 140 \text{ pc}$) if we consider the difference in the distances from the solar system. We note that our model disk is not intended to be representative of any particular source. We discuss this issue further in Section 4.3.

In the top right panel of Figure 7 we show the line profile for the H_2O line at $538.29\mu\text{m}$. The contribution from the outer disk ($r = 14\text{-}30 \text{ au}$) is large compared to that from the optically thick region near the midplane of the inner disk ($r < 14 \text{ au}$) and the width between the double peaks of the line

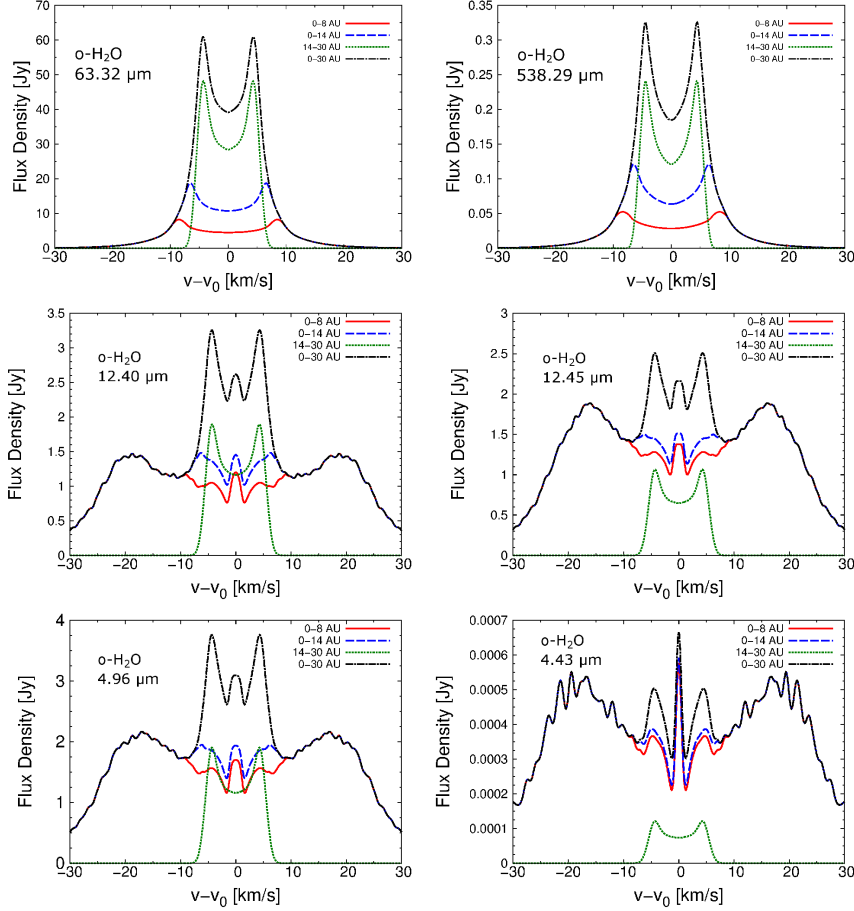


Fig. 7.— (Top two panels): The velocity profiles of two characteristic pure rotational ortho-H₂O lines at $\lambda = 63.32\mu\text{m}$ (top left) and $538.29\mu\text{m}$ (top right) from the Herbig Ae disk. They are examples of lines which are less suited to trace emission from water vapor within the H₂O snowline. (Middle two panels): The velocity profiles of mid-infrared ortho-H₂O lines at $\lambda=12.40\mu\text{m}$ (middle left), $12.45\mu\text{m}$ (middle right) from the Herbig Ae disk. Both lines have much larger values of A_{ul} and E_{up} than those of the candidate mid-infrared H₂O lines to trace the emission from the H₂O vapor within the H₂O snowline. (Bottom two panels): The velocity profiles of near-infrared ortho-H₂O lines at $\lambda=4.96\mu\text{m}$ (bottom left), $4.43\mu\text{m}$ (bottom right) from the Herbig Ae disk. Both lines have the same values of E_{up} ($=4180.4\text{K}$), the former line has a larger value of A_{ul} and the latter line has a smaller value of A_{ul} . *Red solid lines* are the emission line profiles from inside 8 au ($=$ the inner high temperature region), *blue dashed lines* are those from inside 14 au (\sim inside the H₂O snowline), *green dotted lines* are those from 14-30 au (\sim outside the H₂O snowline), and *black dashed dotted lines* are those from the total area inside 30au.

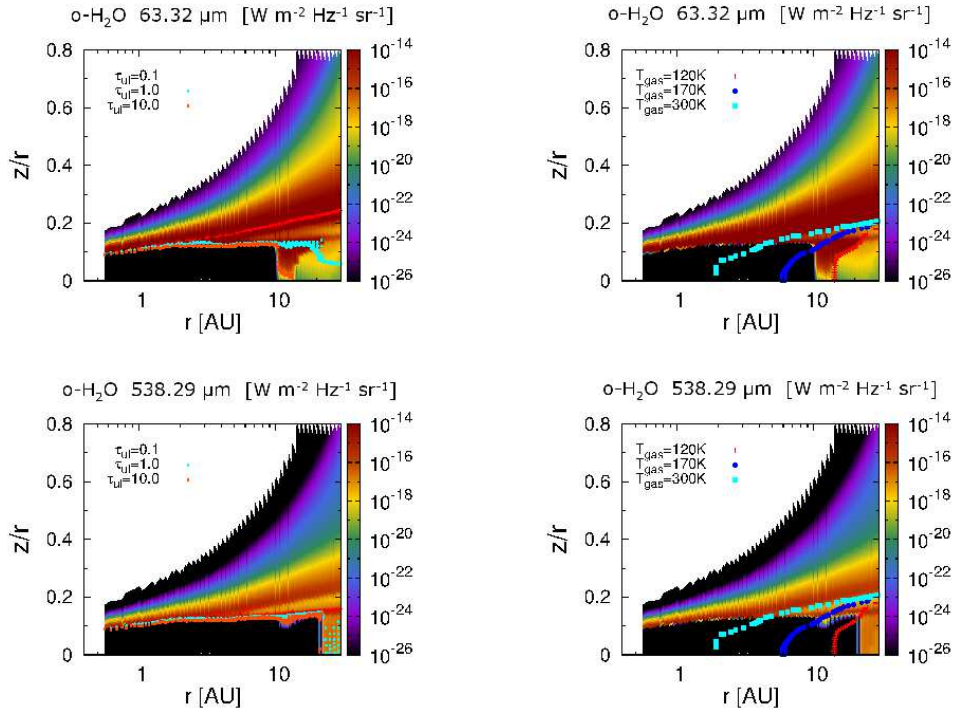


Fig. 8.— The line-of-sight emissivity distributions of the two characteristic H₂O lines at $\lambda=63.32\mu\text{m}$ (top left and right) and $538.29\mu\text{m}$ (bottom left and right), which have various A_{ul} and E_{up} , from the Herbig Ae disk. In the left panels, we overplot the total optical depth contours ($\tau_{ul} = 0.1$ (red cross points), 1 (cyan circle points), and 10 (orange square points)) on top of these line emissivity panels (see also Figure 9). In the right panels, we overplot the gas temperature T_g contours ($T_g = 120\text{K}$ (red cross points), 170K (blue circle points), and 300K (cyan square points), see also Figure 1).

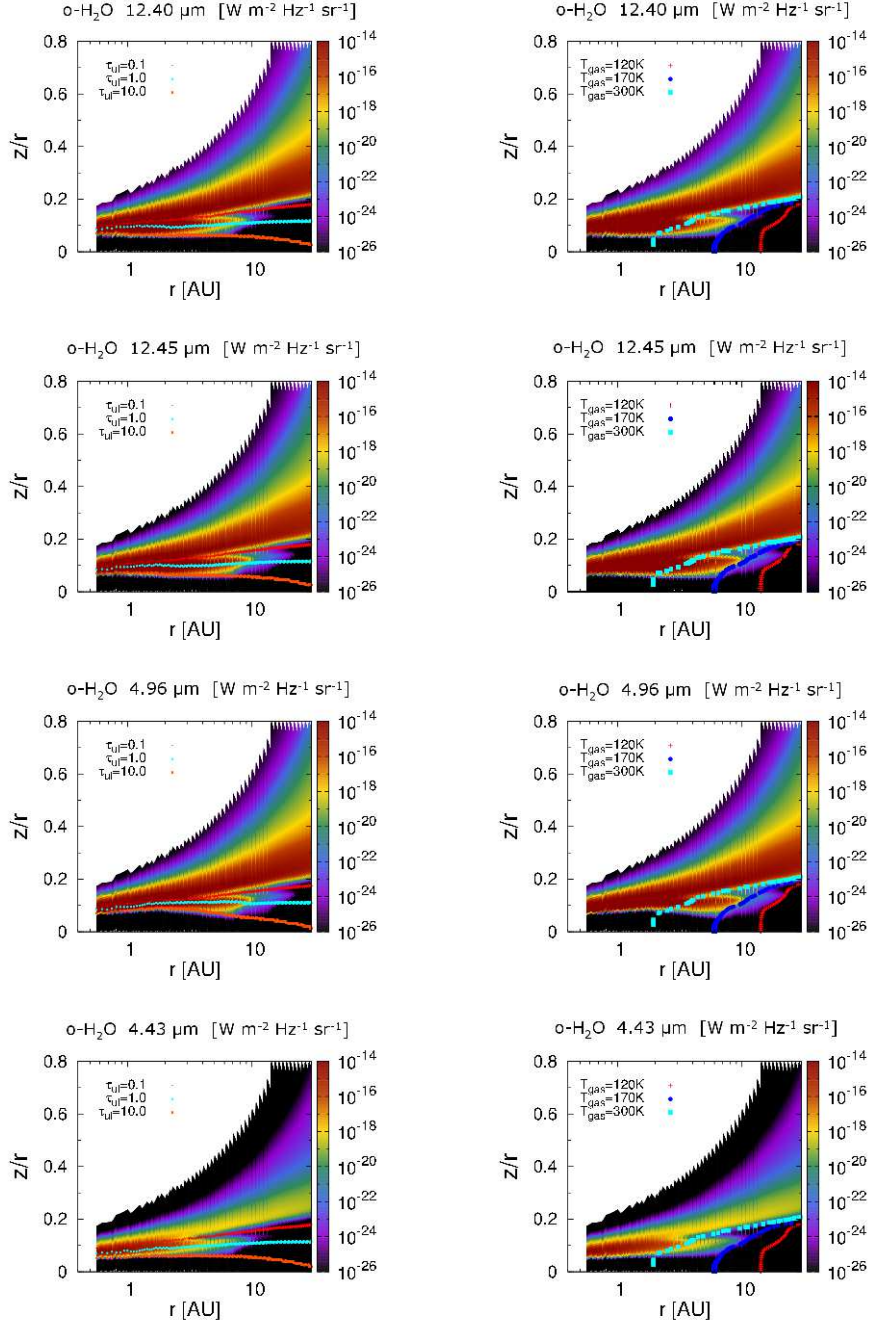


Fig. 8.— (Continued.) (Top and second line panels): The line-of-sight emissivity distributions of mid-infrared H₂O lines at $\lambda=12.40\mu\text{m}$ (top left and right), $12.45\mu\text{m}$ (second line left and right) from the Herbig Ae disk. Both lines have much larger values of A_{ul} and E_{up} than those of the candidate mid-infrared H₂O lines which trace emission from the hot water vapor within H₂O snowline. (Third line and bottom panels): The line-of-sight emissivity distributions of near-infrared H₂O lines at $\lambda=4.96\mu\text{m}$ (third left and right), $4.43\mu\text{m}$ (bottom left and right) from the Herbig Ae disk. Both lines have the same values of E_{up} ($=4180.4\text{K}$), the former line has a larger value of A_{ul} and the latter line has a smaller value of A_{ul} .

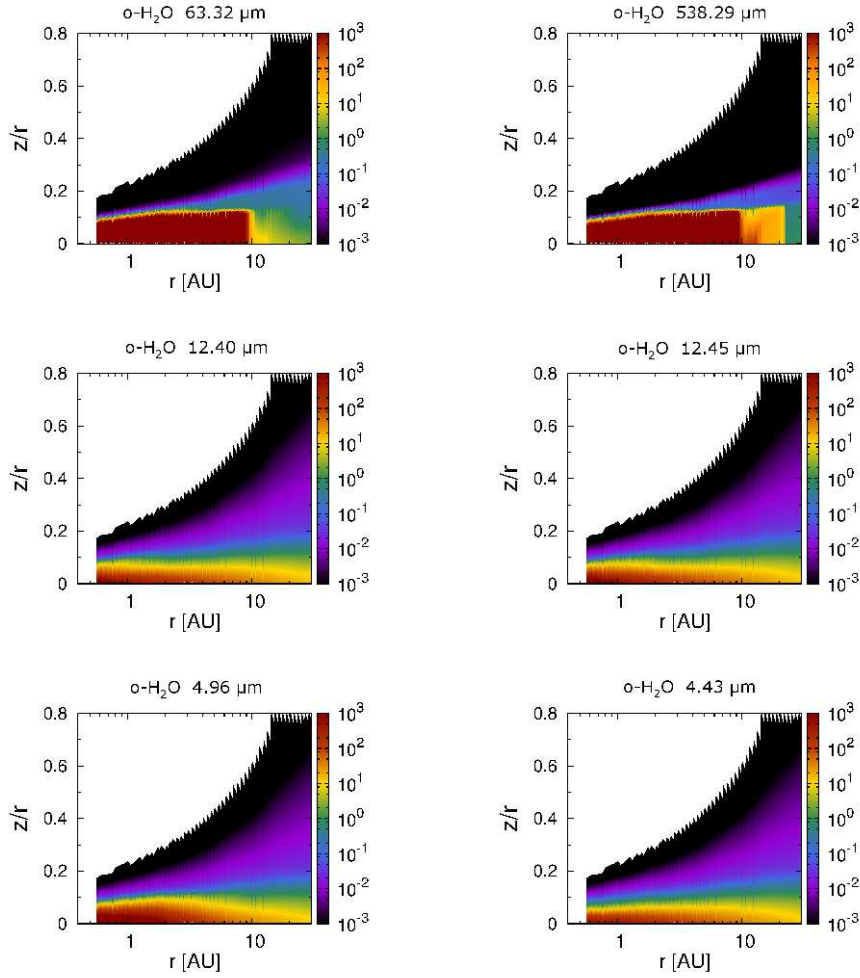


Fig. 9.— (Top two panels): The line-of-sight total optical depth $\tau_{ul}(s, x, y, \nu)$ (gas emission and dust) distributions of two characteristic H₂O lines at 63.32 μ m (top left) and 538.29 μ m (top right) from the Herbig Ae disk. (Middle two panels): The line-of-sight optical depth distributions of mid-infrared ortho-H₂O lines at $\lambda=12.40\mu$ m (middle left), 12.45 μ m (middle right) from the Herbig Ae disk. Both lines have much larger values of A_{ul} and E_{up} than those of the candidate mid-infrared H₂O lines which trace emission from the hot water vapor within H₂O snowline. (Bottom two panels): The line-of-sight optical depth distributions of near-infrared ortho-H₂O lines at $\lambda=4.96\mu$ m (bottom left), 4.43 μ m (bottom right) from the Herbig Ae disk. Both lines have the same values of E_{up} (=4180.4K), the former line has a larger value of A_{ul} and the latter line has a smaller value of A_{ul} .

profile is around two times narrower than those of candidate H₂O lines which trace the emission from the hot water vapor within the H₂O snowline, although the A_{ul} is not so high ($=3.497 \times 10^{-3} \text{s}^{-1}$). This is because this H₂O 538.29 μm line is the ground-state rotational transition and has a low E_{up} ($=61.0\text{K}$) compared with the other lines discussed in this paper. The flux of this line comes mainly from the outer cold water vapor in the photodesorbed layer.

According to Figures 8 and 13, the value of the emissivity of the H₂O 538.29 μm at each (r, z) in the photodesorbed layer is comparable inside and outside the H₂O snowline. However, because of the larger surface area of the outer disk most disk-integrated emission from this line arises from the outer disk. In addition, in the outer disk mid-plane opacity of this line (see Figure 9) is around $10^3 - 10^4$ times higher than those of the ortho-H₂O 482.99 μm and 682.66 μm lines, although the wavelength and thus the dust opacity are similar. This is because this line has a small value of E_{up} and the level population of H₂O for this line is very high near the midplane of cold outer disk. On the basis of these properties, we propose that this line is not optimal to detect emission from the hot water vapor within the H₂O snowline in the Herbig Ae disk case, as also concluded for the T Tauri disk (Notsu et al. 2016).

We mention that previous space high-dispersion spectroscopic observations with *Herschel*/HIFI detected this line from disks around one Herbig Ae star HD100546 and two T Tauri stars TW Hya and DG Tau (e.g., Hogerheijde et al. 2011; Podio et al. 2013; van Dishoeck et al. 2014; Salinas et al. 2016). The number of detections is small because the line flux is low compared with the sensitivity of that instrument (Antonellini et al. 2015). The detected line profile and other line modeling work (e.g., Meijerink et al. 2008; Woitke et al. 2009b; Antonellini et al. 2015) suggested that the emitting region arises in the cold outer disk, consistent with the results of our model calculations.

Here we note that since we define $\text{OPR} = 3$ (=the value in the high temperature region) throughout the disk, we may be overestimating the line flux

of the ortho-H₂O 538.29 μm line (for more details, see Section 2.3 of paper I, Notsu et al. 2016). In addition, since the flux of this line is controlled by the outer cold H₂O gas which is desorbed from the cold dust-grain surfaces, it also may be necessary to include grain-surface reactions (e.g., Hasegawa et al. 1992) for accurate determination of the gas phase H₂O abundance in this region.

The middle two panels of Figure 7 show the profiles for the pure rotational mid-infrared ortho-H₂O lines at $\lambda=12.40\mu\text{m}$ (middle left), 12.45 μm (middle right) from the Herbig Ae disk. Figures 8, 9, and 13 also show the line-of-sight emissivity, the total optical depth (gas emission and dust), and the vertical normalized cumulative emissivity distributions of these two mid-infrared H₂O lines from the Herbig Ae disk, respectively. Both lines have much larger values of A_{ul} ($>1 \text{s}^{-1}$) and E_{up} ($>4000\text{K}$) than those of the candidate mid-infrared H₂O lines that trace emission from the H₂O vapor within the H₂O snowline in the disk midplane (see Table 1 and B.1), and thus they mainly trace emission from the hot surface of the inner and outer disk. The velocity profiles of these two lines were obtained by previous ground-based mid-infrared spectroscopic observations using VLT/VISIR (Pontoppidan et al. 2010b) from bright T Tauri disks (AS 205N and RNO 90). They show the Keplerian double-peaked or flat-topped (for low inclination objects) profiles, and the line emitting region is the hot disk surface.

The bottom two panels of Figure 7 show the profiles of pure rotational near-infrared ortho-H₂O lines at $\lambda=4.96\mu\text{m}$ (bottom left), 4.43 μm (bottom right) from the Herbig Ae disk. Figures 8, 9, and 13 also show the line-of-sight emissivity, the total optical depth (gas emission and dust), and the vertical normalized cumulative emissivity distributions of these near-infrared lines for the Herbig Ae disk, respectively. Both lines have the same much larger values of E_{up} ($=4180.4\text{K}$), the former line has a larger value of A_{ul} ($=3.260 \text{s}^{-1}$) and the latter has a smaller value of A_{ul} ($=2.080 \times 10^{-4} \text{s}^{-1}$). For the former case, since it has much larger values of A_{ul} and E_{up} than those of the candidate H₂O lines (see Table 1 and B.1), it mainly traces the emission from the hot surface of the inner and outer disk. This line has similar values

of A_{ul} and E_{up} with the observed near-infrared rovibrational H₂O lines in L band (Mandell et al. 2012). For the latter smaller A_{ul} line case, since the value of E_{up} in this near-infrared line is much larger ($>4000\text{K}$) than those of the candidate H₂O lines which trace the emission from the hot water vapor within the H₂O snowline from mid-infrared to sub-millimeter wavelengths, it only traces the very innermost region ($r < 3$ au for the $4.43\mu\text{m}$ line case). In addition, the widths between the two peaks of the Keplerian profiles of these near- and mid-infrared lines with large E_{up} are larger than those of candidate H₂O lines which trace the emission from the hot water within the H₂O snowline (see Figures 4, 7, and 14). These are because they trace the innermost hot region compared with the region around the H₂O snowline.

Here we note that previous near- and mid-infrared spectroscopic observations using VLT/CRIRES and *Spitzer*/IRS for Herbig Ae disks (e.g., Pontoppidan et al. 2010a; Fedele et al. 2011; Salyk et al. 2011) have not detected any H₂O lines regardless of the value of A_{ul} . We discuss this issue in Section 4.3. Moreover, as we described in Section 2.3, the level populations of the water molecule are calculated under LTE, as opposed to non-LTE. However, as we discuss further in Section 4.2, in our LTE calculations there is a possibility that we have overestimated the emission fluxes of strong H₂O lines with large A_{ul} which trace the hot surface layer, as found in previous studies (e.g., Meijerink et al. 2009; Woitke et al. 2009b; Banzatti et al. 2012; Antonellini et al. 2015).

3.2.3. The total fluxes of candidate H₂O emission lines which trace emission from the hot water vapor within H₂O snowline

Figure 10 shows the total fluxes of the various ortho-H₂O lines which are the candidates for tracing emission from hot water vapor within the H₂O snowline for a Herbig Ae disk (top panel) and a T Tauri disk (bottom panel). We select those lines from the LAMDA database (see Section 2.3 of paper I, Notsu et al. 2016) which have both small values of A_{ul} ($10^{-6} < A_{ul} < 10^{-2} \text{ s}^{-1}$) and relatively large values of E_{up} ($700 < E_{up} < 2100\text{K}$). The wavelengths of these lines range from mid-infrared to sub-millimeter, $\lambda \sim 11 - 1000\mu\text{m}$, be-

cause we do not have candidate lines which trace emission from the hot water vapor within H₂O snowline with wavelengths $\lambda < 10\mu\text{m}$ on the basis of our criteria for A_{ul} and E_{up} . The values of E_{up} of lines for wavelengths $\lambda < 10\mu\text{m}$ are too large ($\gtrsim 3000\text{K}$), and the opacity of the dust grains for wavelengths $\lambda < 10\mu\text{m}$ is expected to be too large to trace the emission from the midplane of the disk (see Sections 3.2.2 and 4.3). The detailed parameters, such as transitions ($J_{K_a K_c}$), wavelength, frequency, A_{ul} , E_{up} , and total line fluxes of these candidate ortho-H₂O lines shown in Figure 10 are listed in Table B.1 of Appendix B. In Figure 10 and Table B.1, we show both values for the total fluxes from the Herbig Ae disk and the T Tauri disk. In addition, Figure 14 in Appendix C shows the profiles of mid-infrared candidate lines ($\lambda \sim 11 - 25\mu\text{m}$) for the Herbig Ae disk. All lines in this Figure are listed in Table B.1.

On the basis of Figure 10, Figure 14, Table 1, and Table B.1, the values of fluxes of these lines from the Herbig Ae disk are around $10^2 - 10^3$ larger than those of the T Tauri disk. This is because the position of the H₂O snowline in the Herbig Ae disk exists at a larger radius from the central star than that in the T Tauri disk. In addition, the peak fluxes of these lines become larger as the values of A_{ul} become larger and E_{up} become smaller. Moreover, the values of total flux tend to be larger as the wavelengths of these H₂O lines become shorter. This is because the peak wavelengths of the Planck function at the gas temperatures around the H₂O snowline ($T_g \sim 100\text{-}200 \text{ K}$) are at mid-infrared wavelengths. In the cases of the Herbig Ae disk and the T Tauri disk, the values of total fluxes of the mid-infrared H₂O lines which trace emission from the hot water vapor within H₂O snowline are $\sim 10^2 - 10^4$ and $\sim 10^1 - 10^2$ times larger than those of sub-millimeter H₂O lines, respectively, and there are differences in the line flux ratio of mid-infrared lines to sub-millimeter lines between the Herbig Ae and the T Tauri disks. These are because the amount of hot H₂O gas around the region at $\tau_{ul} \lesssim 1$ in mid-infrared lines and inside the H₂O snowline are higher in the Herbig Ae disk model than that in the T Tauri disk.

On the basis of Figure 14, most of the emission

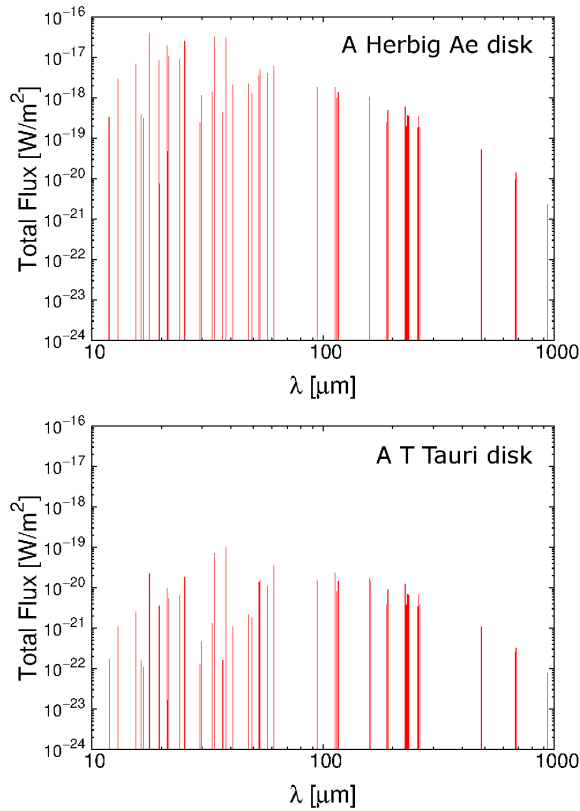


Fig. 10.— The total fluxes of the ortho-H₂O lines which are best candidates to trace the emission from the water vapor within the H₂O snowline, for a Herbig Ae disk (top panel) and a T Tauri disk (bottom panel). We select these lines based on their small Einstein A coefficients of $10^{-6} < A_{ul} < 10^{-2} \text{ s}^{-1}$ and relatively large excitation energies of $700 < E_{up} < 2100\text{K}$. The wavelengths of these lines range from mid-infrared to sub-millimeter, $\lambda \sim 11 - 1000\mu\text{m}$.

flux from these mid-infrared lines comes from the region with a high H₂O gas abundance ($\sim 10^{-4}$, $r < 8 \text{ au}$), and the position of the two peaks and the rapid drop in flux density between the peaks contains information on the position of the outer edge of this region. This is because they have shorter wavelengths ($\lambda \sim 11 - 25\mu\text{m}$) and relatively larger values of E_{up} ($\sim 1500 - 2000\text{K}$ except for the H₂O 17.75 and 24.00 μm lines) among all candidate lines which trace the emission from the hot H₂O vapor within the H₂O snowline (see Table B.1).

3.2.4. The radial distributions of normalized cumulative line fluxes

Figure 11 shows the normalized radial cumulative fluxes for seven H₂O lines at $\lambda=682.66\mu\text{m}$, $63.32\mu\text{m}$, $538.29\mu\text{m}$, $12.40\mu\text{m}$, $12.45\mu\text{m}$, $4.96\mu\text{m}$, and $4.43\mu\text{m}$. We discussed the properties of these seven lines in Sections 3.2.1 and 3.2.2. According to these figures, around 90% of the flux of the $682.66\mu\text{m}$ line is emitted from the region inside the H₂O snowline ($r < 14 \text{ au}$). In contrast, emission from the $63.32\mu\text{m}$ and the $538.29\mu\text{m}$ lines is emitted mostly from the region outside the H₂O snowline. In addition, although the $63.32\mu\text{m}$ line is mainly emitted from the region between $r \sim 25 - 200 \text{ au}$, the $538.29\mu\text{m}$ line is mainly emitted from a region much further out ($r \sim 50 - 300 \text{ au}$). The properties of these three lines for the Herbig Ae disk are similar to those for the T Tauri disk which we showed and discussed in Figure 7 and Section 3.2.5 in paper I (Notsu et al. 2016).

The $12.40\mu\text{m}$, $12.45\mu\text{m}$, and $4.96\mu\text{m}$ lines are mainly emitted both from the regions within 3 au and outside the H₂O snowline ($r > 14 \text{ au}$). The emission from the region between 3-14au (= the H₂O snowline) is much smaller. The $4.43\mu\text{m}$ line is mainly emitted from the innermost region of the disk ($r < 3 \text{ au}$). These are because these four lines have much larger values of E_{up} ($> 4000\text{K}$) than both the candidate H₂O lines that trace the hot water vapor within the H₂O snowline and the $63.32\mu\text{m}$ line. Thus, the values of flux densities from the hot surface layer of the inner disk are larger. The $4.43\mu\text{m}$ line has a smaller value of A_{ul} ($= 2.080 \times 10^{-4} \text{ s}^{-1}$) and thus the values of flux densities from the hot surface layer of the outer

disk are much smaller, but the other three lines have larger values of A_{ul} ($>1 \text{ s}^{-1}$) and thus the values of flux densities from the hot surface layer of the outer disk are larger.

Figure 12 shows the normalized radial cumulative fluxes for seven rotational ortho- H_2O lines that trace the hot water vapor within the H_2O snowline: $\lambda=17.75\mu\text{m}$, $24.00\mu\text{m}$, $61.32\mu\text{m}$, $94.17\mu\text{m}$, $482.99\mu\text{m}$, $682.66\mu\text{m}$, and $933.28\mu\text{m}$. We discussed the properties of these seven lines in Sections 3.2.1 and 3.2.3. In the cases of the H_2O $482.99\mu\text{m}$ and $682.66\mu\text{m}$ lines, most of the flux is emitted from the region with a high H_2O gas abundance ($\sim 10^{-4}$, $r < 8 \text{ au}$), with some emission flux emitted from the region with a relatively high H_2O gas abundance ($\sim 10^{-8}$, $r = 8\text{-}14 \text{ au}$). On the other hand, for the other H_2O lines, almost all of the emission flux comes from the region with a high H_2O gas abundance ($\sim 10^{-4}$, $r < 8 \text{ au}$). Such differences in line properties come from the differences in E_{up} and the dust opacity at different wavelengths. The H_2O $482.99\mu\text{m}$ and $682.66\mu\text{m}$ lines have relatively smaller values of E_{up} ($< 1100\text{K}$) and longer wavelengths ($> 400\mu\text{m}$), as discussed in Section 3.2.1. In Figure 12, lines which have larger E_{up} and shorter wavelengths tend to be emitted from the innermost region within the H_2O snowline.

4. Discussion

4.1. Influence of model assumptions on the properties of H_2O emission lines

In Section 3.2.4 of paper I (Notsu et al. 2016), we discussed the uncertainties in our model predictions in detail, and we also discussed the behavior of the H_2O lines for some cases in which we artificially changed the distribution of H_2O vapor, the position of the H_2O snowline, and the fractional abundance of H_2O gas in the outer disk surface layer (see Figures 8 and 9 of paper I, Notsu et al. 2016). We explored different values of the H_2O snowline radius to simulate the effects of (i) increased and decreased viscous heating (e.g., Oka et al. 2011; Harsono et al. 2015), (ii) using different dust opacities due to dust-grain growth (e.g., Aikawa & Nomura 2006; Oka et al. 2011). We varied the abundance of water vapor in the

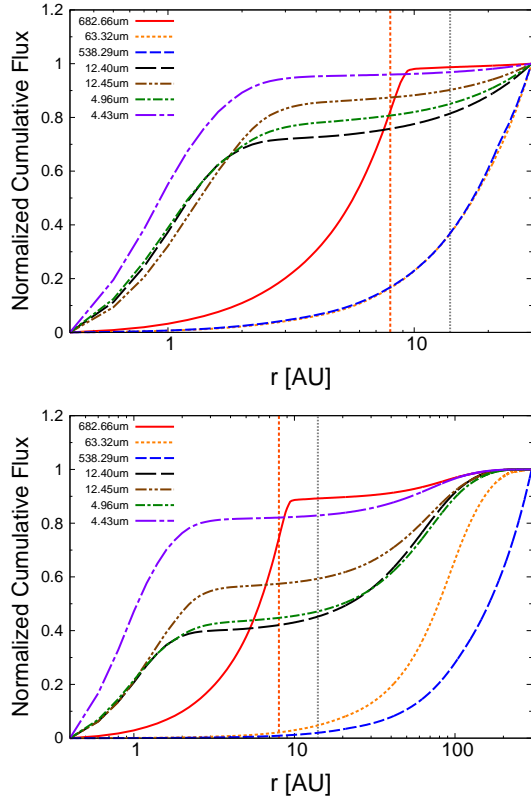


Fig. 11.— The radial distributions of the normalized cumulative flux for seven pure rotational ortho- H_2O lines at $\lambda=682.66\mu\text{m}$ (*red solid line*), $63.32\mu\text{m}$ (*orange dotted line*), $538.29\mu\text{m}$ (*blue dashed line*), $12.40\mu\text{m}$ (*black long dashed line*), $12.45\mu\text{m}$ (*brown dashed two dotted line*), $4.96\mu\text{m}$ (*green dashed dotted line*), and $4.43\mu\text{m}$ (*violet long dashed dotted line*). The vertical straight lines display the positions of $r=8 \text{ au}$ (*orange dotted line*) and 14 au (*grey dotted line*), respectively. We normalized the cumulative flux of each line using the values at $r = 30 \text{ au}$ (top panel) and at $r = 300 \text{ au}$ (bottom panel). We assume that the inclination angle of the disk i is 0 degree in making these figures.

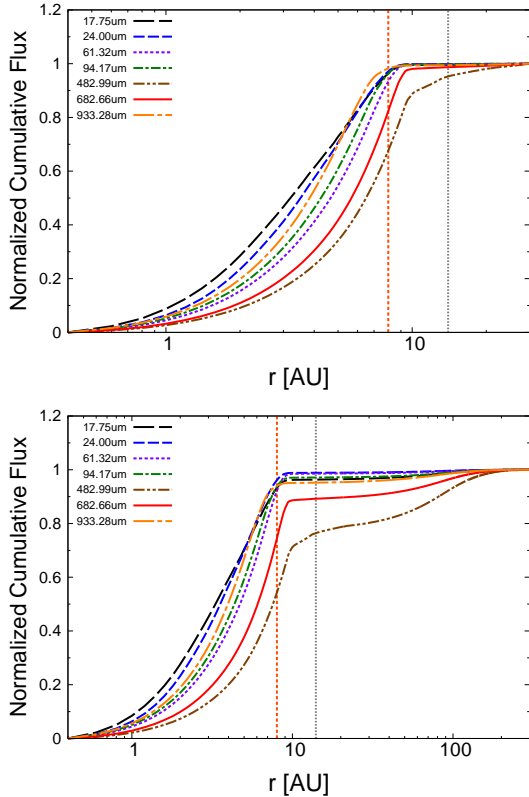


Fig. 12.— The radial distributions of the normalized cumulative flux for seven pure rotational ortho- H_2O lines at $\lambda=17.75\mu\text{m}$ (*black long dashed line*), $24.00\mu\text{m}$ (*blue dashed line*), $61.32\mu\text{m}$ (*violet dotted line*), $94.17\mu\text{m}$ (*green dashed dotted line*), $482.99\mu\text{m}$ (*brown dashed two dotted line*), $682.66\mu\text{m}$ (*red solid line*), and $933.28\mu\text{m}$ (*orange long dashed dotted line*). These are candidate ortho- H_2O lines to trace the emission from the hot water vapor within the H_2O snowline. The vertical straight lines display the positions of $r=8$ au (*orange dotted line*) and 14 au (*grey dotted line*), respectively. We normalized the cumulative flux of each line using the values at $r = 30$ au (top panel) and at $r = 300$ au (bottom panel). We assume that the inclination angle of the disk i is 0 degree in making these figures.

disk atmosphere to simulate the effects of (iii) increasing/decreasing the strength of UV photoreactions. We found that in the cases for which the H_2O snowline is more distant from the central star, and the fractional abundance of H_2O gas in the disk atmosphere is lower than that in the originally adopted T Tauri disk, the line fluxes from the hot inner disk midplane inside the H_2O snowline are more dominant from those from the outer disk (e.g., Walsh et al. 2012).

An analysis of spectral energy distributions (SEDs) classified Herbig Ae/Be stars into two groups (group I/II, Meeus et al. 2001). Group I sources show both power-law and blackbody components up to far-infrared wavelengths in their SEDs. SEDs of group II sources can be well modeled with only a single power law from mid- to far-infrared wavelengths. Meeus et al. (2001) suggested that group I sources have a flaring disk while the group II disks are geometrically flat. Meeus et al. (2001) proposed a possible evolutionary scenario where a group I flaring disk evolves into a group II flat disk through grain growth and settling of grains onto the disk midplane (see also Dominik et al. 2003; Dullemond & Dominik 2004).

However, recent high-spatial resolution observations at various wavelengths have revealed a more complex structure in disks, with inner holes and/or gaps toward many group I sources such as HD100546 (e.g., Benisty et al. 2010; Panić et al. 2014; Walsh et al. 2014b), HD142527 (e.g., Fujiwara et al. 2006; Fukagawa et al. 2006, 2013), and HD169142 (e.g., Benisty et al. 2010; Honda et al. 2012). On the other hand, there is little evidence for inner holes and/or gaps reported toward group II disks, and they seem to have a radially continuous structure (e.g., Honda et al. 2015). Honda et al. (2012) and Maaskant et al. (2013) suggested that most group I sources can be classified as (pre-)transitional disks. Transitional and pre-transitional disks are protoplanetary disks with an inner hole and/or gaps indicated by a lack of near-infrared/mid-infrared excess in their SEDs (e.g., Strom et al. 1989; Espaillat et al. 2007). They pointed out that there is no significant difference in age between groups I and II sources (Meeus et al. 2001; Honda et al. 2015). Therefore, recent studies (e.g., Maaskant et al.

2013; Honda et al. 2015) suggested that both group I and II sources had experienced different evolutionary paths from some common primordial and continuous flaring disks. Here we note that Menu et al. (2015), Isella et al. (2016), and Zhang et al. (2016) suggested that some geometrically flat disks (group II disk) have gaps. Menu et al. (2015) suggested flat disks with gaps are most likely descendants of flat disks without gaps. Banzatti et al. (2016) discovered a correlation between water line fluxes at $\lambda = 2.9\mu\text{m}$ and $10 - 33\mu\text{m}$ and the size of inner disk gaps/holes as probed by $4.7\mu\text{m}$ CO rovibrational emission lines. They described that the lower detection frequency of near- and mid-infrared water vapor lines in disks around intermediate mass stars ($M_* = 1.5 - 4M_\odot$) is linked to inner gaps/holes with depleted molecular gas content of the disks out to close to or beyond the H_2O snowline.

Our Herbig Ae disk model adopted in this paper has a radially continuous structure with no inner hole and/or gap. If we adopt a disk model with an inner hole and/or gap, the emission fluxes of H_2O lines, especially from the hot water vapor inside the H_2O snowline is expected to decrease. Recently ALMA observations with high spatial resolution have been conducted towards protoplanetary disks with various central star masses/ages (e.g., ALMA Partnership et al. 2015; Andrews et al. 2016; Isella et al. 2016; Tsukagoshi et al. 2016), and will help understand these evolutionary scenarios.

4.2. Critical density and the assumption of LTE

In this subsection, we discuss the validity of the assumption of LTE. As we discussed in paper I (Notsu et al. 2016), the assumption of LTE is valid in calculating the emission flux of the $682.66\mu\text{m}$ line. This is because this line mainly comes from the hot region around $z/r \sim 0.1$ within the H_2O snowline where the total gas density ($\sim 10^{11} - 10^{14} \text{ cm}^{-3}$) is much larger than the critical density for this line ($n_{\text{cr}} = 1.0 \times 10^6 \text{ cm}^{-3}$, see also Table 1). On the other hand, in our LTE calculations it remains possible that we have overestimated the emission flux of strong H_2O lines with large A_{ul} ($\sim 10^{-1} - 10^0 \text{ s}^{-1}$) which trace the hot surface layer

of the inner/outer disk (e.g., the $12.40 \mu\text{m}$ and the $63.32 \mu\text{m}$ lines) and lines which trace the cold water vapor in the photodesorbed layer (e.g., the $538.29 \mu\text{m}$ line). The values of n_{cr} of these lines (e.g., $n_{\text{cr}} = 1.1 \times 10^{11}$, 1.5×10^{10} , and $2.9 \times 10^7 \text{ cm}^{-3}$ for the $12.40 \mu\text{m}$, the $63.32 \mu\text{m}$, and the $538.29 \mu\text{m}$ lines, respectively) are larger than or similar to the total gas density in the hot surface layer of the inner/outer disk ($\sim 10^7 - 10^8 \text{ cm}^{-3}$) and the photodesorbed layer ($\sim 10^8 - 10^{10} \text{ cm}^{-3}$). Previous studies which model such H_2O lines (e.g., Meijerink et al. 2009; Woitke et al. 2009b; Banzatti et al. 2012; Antonellini et al. 2015, 2016) showed that non-LTE calculations are important for the latter lines. They suggested that non-LTE effects may, however, alter line fluxes by factors of only a few for moderate excitation lines ($E_{\text{up}} < \text{a few thousand K}$). Moreover, current non-LTE calculations are likely to remain inaccurate, due to the incompleteness and uncertainty of collisional rates (e.g., Meijerink et al. 2009; Banzatti et al. 2012; Kamp et al. 2013; Zhang et al. 2013; Antonellini et al. 2015).

We calculated the critical density n_{cr} of the six other lines discussed in Section 3.2.1 and Figures 4, 5, and 6 as probes interior to the H_2O snowline (the 17.75 , 24.00 , 61.32 , 94.17 , 482.99 , and $933.28 \mu\text{m}$ lines, see Table 1). n_{cr} for the sub-millimeter lines at 482.99 , 682.66 , and $933.28 \mu\text{m}$ (3.3×10^6 , 1.0×10^6 , and $4.7 \times 10^6 \text{ cm}^{-3}$, respectively) are lower than the values of the total gas density in the hot surface layer of the outer disk ($\sim 10^7 - 10^8 \text{ cm}^{-3}$) and in the photodesorbed water layer ($\sim 10^8 - 10^{10} \text{ cm}^{-3}$). In contrast, n_{cr} for the mid- to far-infrared lines (8.3×10^{10} , 1.9×10^9 , 4.1×10^8 , and $3.1 \times 10^8 \text{ cm}^{-3}$ for the 17.75 , 24.00 , 61.32 , and $94.17 \mu\text{m}$ lines, respectively) are similar to and larger than the values of the total gas density in those regions. This is because the latter infrared lines have larger Einstein A coefficients and shorter wavelengths compared with the aforementioned sub-millimeter lines. If the wavelength of a line is shorter, the energy difference between the upper and lower state is larger and the value of collisional rates $\langle \sigma v \rangle$ tends to be smaller (Faure & Josselin 2008). However, emission from these lines mainly comes from the hot water vapor within the H_2O snowline where total gas density is much larger ($\sim 10^{11} - 10^{14} \text{ cm}^{-3}$) than the values

of n_{cr} , and thus it is valid to use LTE to calculate their fluxes.

4.3. Previous H₂O line observations in Herbig Ae disks

Since H₂O line emission from the disk midplane is likely obscured by dust grains at near- to mid-infrared wavelengths (Walsh et al. 2015), the “visible” H₂O gas column density at these wavelengths is smaller than the total H₂O column density integrated over the disk in the vertical direction (see e.g., Figure 3). For example, in Walsh et al. (2015), the visible column density at 14 μm in the Herbig Ae disk case is $\sim 10^{19} - 10^{20} \text{ cm}^{-2}$ within the H₂O snowline. In the bottom panel of Figure 3, the visible H₂O gas column densities at 17.75, 61.32, and 682.66 μm in the Herbig Ae disk are $\sim 10^{18} - 10^{19} \text{ cm}^{-2}$ within the H₂O snowline, which are lower than those of Walsh et al. (2015). This is because the total integrated column density of water vapor in our model ($\sim 10^{20} - 10^{22} \text{ cm}^{-2}$) is lower than that of Walsh et al. (2015) ($\sim 10^{21} - 10^{23} \text{ cm}^{-2}$), and because absorption by dust grains is dominant in the disk midplane and the disk surface ($\tau_{\text{ul}} \lesssim 1$) compared to that by excited gas molecules, especially remarkable in the cases of infrared lines (see also Section 3.2.1). Previous near- and mid-infrared spectroscopic observations using instruments on ground and space telescopes (e.g., VLT/CRIRES and *Spitzer*/IRS) for Herbig Ae disks (Pontoppidan et al. 2010a; Fedele et al. 2011; Salyk et al. 2011) have not detected the H₂O lines, and they derive upper limits for H₂O gas column densities ($\lesssim 10^{18} \text{ cm}^{-2}$). However, such near- and mid-infrared H₂O lines are observed in many T Tauri disks (e.g., Pontoppidan et al. 2010a, see also Section 1 of paper I, Notsu et al. 2016). H₂O lines at far-infrared wavelengths have been detected with *Herschel*/PACS only in the disk around HD163296, although this emission originates in the hot surface layer of the outer disk ($r > 15 \text{ au}$), and it is farther out than that expected for emission at shorter wavelengths (Fedele et al. 2012, 2013; Meeus et al. 2012). From these observational results, there is an important question as to why the detection rate for near- and mid-infrared H₂O lines for T Tauri disks is higher than that for Herbig Ae disks.

Previous studies (e.g., Voitke et al. 2009b; Pontoppidan et al. 2010a; Fedele et al. 2011; Meeus et al. 2012; Walsh et al. 2015; Antonellini et al. 2015, 2016) discussed some answers to the above question. Here we highlight some important ideas (see also Section 3.2.2). First, there may be additional destruction routes for gas-phase water in the inner disk atmosphere, not yet included in the chemical networks we have adopted, for example the reaction to produce OH via photodissociation of H₂O by Lyman- α photons (Walsh et al. 2015). Second, dust-grain settling and dust-grain growth can reduce the total dust-grain surface area and possibly increase the UV irradiation rates in the upper disk (e.g., Vasyunin et al. 2011; Akimkin et al. 2013), which can push the molecular layer deeper into the disk atmosphere. Hence, a higher fraction of the gas-phase water may be hidden from view (e.g., Walsh et al. 2015; Krijt et al. 2016). We note that HD100546, for which far-infrared H₂O lines have not been detected, has very high UV flux from the central star and even at 30 au the UV field is expected to be too strong for gas-phase water to survive (Meeus et al. 2012). Tilling et al. (2012) modeled the disk of HD163296 and pointed out that the dust material is settled. Meanwhile, dust-grain growth and the dust-grain shape also affect the UV field through scattering efficiency in the disk atmosphere. If the dust-grain radius is large enough compared with the wavelength of radiation from the central star, forward scattering by dust grains becomes efficient and the UV field decreases in the disk atmosphere (e.g., Bethell & Bergin 2011). The gas temperature in the disk atmosphere, which affects the H₂O line fluxes, is also controlled by the UV radiation field. If the UV radiation field increases/decreases, the gas temperature in the disk atmosphere will become higher/lower. We have assumed isotropic dust scattering and the grain size distribution of the dark cloud model with compact and spherical dust grains (For more details, see Nomura & Millar 2005 and paper I, Notsu et al. 2016), and these assumptions will affect the resulting H₂O line fluxes. Third, if the disk is transitional and has a significant gap/hole in the inner disk (e.g., HD100546), the line fluxes from the inner disk atmosphere will be decreased (e.g., Banzatti et al. 2016, see also Section 4.1).

Fourth, in Herbig Ae disks the strong infrared excess of dust emission might veil the faint emission of molecular lines at infrared wavelengths (e.g., Lahuis et al. 2007; Pontoppidan et al. 2010a; Fedele et al. 2011; Antonellini et al. 2015, 2016). Previous line modeling calculations such as Du & Bergin (2014) and Antonellini et al. (2015, 2016) concluded the infrared and sub-millimeter water line fluxes are affected by many parameters related to disk physical structure, such as dust-size distribution, dust-to-gas mass ratio, disk gas mass, maximum dust size, and luminosity of the central star. Antonellini et al. (2015, 2016) showed that the sensitivity and spectral resolution of previous mid-infrared observations (e.g., *Spitzer*/IRS) were not sufficient to detect the detailed profiles of even strong H₂O lines (with large A_{ul}) in many disks, especially disks around high-mass Herbig Ae/Be stars. This was because of the presence of noise in the spectra which can mask the line emission, combined with the high dust continuum flux (the noise level is proportional to the dust continuum flux).

4.4. Requirement for the observations of candidate H₂O lines to trace the H₂O snowline

Since the velocity width between the emission peaks is ~ 20 km s⁻¹, high-dispersion spectroscopic observations ($R=\lambda/\delta\lambda >$ tens of thousands) of the H₂O lines in Table B.1 are needed to trace emission from the hot water vapor within the H₂O snowline. Their profiles contain information which can be used to locate the position of the H₂O snowline. The area of the emitting regions are small ($r < 2$ au for a T Tauri disk and $r < 14$ au for a Herbig Ae disk) compared with the total disk size. The spectral resolution (of many instruments) and sensitivity used for previous mid-infrared, far-infrared, and sub-millimeter observations (e.g., *Spitzer*/IRS, *Herschel*/PACS, *Herschel*/HIFI) were not sufficient to detect and resolve the candidate lines we identified in Table B.1 which trace emission from the hot water vapor within H₂O snowline.

Among the various H₂O lines in ALMA band 8, the H₂O 682.66 μ m line is the most suitable to

trace emission from the hot water vapor within the H₂O snowline. Other candidate sub-millimeter H₂O lines to trace the H₂O snowline, having the same order-of-magnitude fluxes, exist in ALMA bands 7, 9 and 10 ($\sim 300 - 1000$ μ m). The H₂O 933.28 μ m and 482.99 μ m lines are the most suitable lines in ALMA band 7 and 9, respectively. Here we note that although there is no candidate ortho-H₂O line in ALMA band 10, some candidate para-H₂O lines do fall in this band. With ALMA, we can now conduct high sensitivity ($\sim 10^{-21} - 10^{-20}$ W m⁻² (5σ , 1 hour)), high-dispersion ($R > 100,000$), and even high spatial resolution (< 100 mas) spectroscopic observations. Since the total fluxes of the candidate sub-millimeter lines which trace the emission from hot water vapor within the H₂O snowline are low in T Tauri disks ($\sim 10^{-22} - 10^{-21}$ W m⁻²), they remain challenging to detect with current ALMA sensitivity unless we have an unrealistically long integration time (see paper I, Notsu et al. 2016). However, in hotter Herbig Ae disks, in younger T Tauri disks (e.g., HL Tau, ALMA Partnership et al. 2015; Banzatti et al. 2015; Harsono et al. 2015; Zhang et al. 2015; Okuzumi et al. 2016), and in disks around FU Orionis type stars (e.g., V883 Ori, Cieza et al. 2016), the H₂O snowline exists at a larger radius and the fluxes of these lines will be stronger compared with those in our fiducial T Tauri disk.

Our calculations for a Herbig Ae disk predict the fluxes of the 482.99 μ m (band 9), 682.66 μ m (band 8), and 933.28 μ m (band 7) lines to be around $10^{-21} - 10^{-20}$ W m⁻² if we assume that the distance to the object d is 140pc (\sim the distance of Taurus molecular cloud), and the inclination angle of the disk i is 30 deg. Thus the possibility of a successful detection is expected to increase in such Herbig Ae disks and could be achieved with current ALMA capabilities. Here we mention that the 933.28 μ m line has been detected with high spectral resolution in the disk and outflow around the massive protostar candidate, Source I in Orion KL (Hirota et al. 2014), using ALMA, and around the embedded low mass protostar (Class I), HL Tau, using SMA (Kristensen et al. 2016). Kristensen et al. (2016) suggested that future observations at higher sensitivity and angular resolution with ALMA will clarify the origin of this

water emission from HL Tau and resolve the disk structures.

Candidate H₂O lines to trace the H₂O snowline exist over a wide wavelength range, from mid-infrared to sub-millimeter. As we discuss in Section 3.2.3, the values of the total fluxes tend to increase as the wavelengths of the candidate H₂O lines which trace emission from the hot water vapor within H₂O snowline become shorter (see Table 1, B.1, and Figure 10). There are future mid-infrared instruments covering the part of Q band which will enable high sensitivity and high-dispersion spectroscopic observations: the HRS on SPICA⁶ Mid-infrared Instrument (SPICA/SMI) and Mid-Infrared Camera High-disperser & IFU spectrograph on the Thirty Meter Telescope (TMT/MICHI, e.g., Packham et al. 2012). HRS on SPICA/SMI will have a relatively high spectral resolution ($R \sim 28,000$), and especially high sensitivity ($\sim 10^{-20} \text{ W m}^{-2}$ (5σ , 1 hour)) compared with previous mid-infrared instruments at the same wavelengths. TMT/MICHI will have a high spectral resolution ($R \sim 60,000\text{--}120,000$), high sensitivity ($\sim 10^{-19} \text{ W m}^{-2}$ (5σ , 1 hour)). The H₂O 17.75 μm and 24.00 μm lines are in the Q band at mid-infrared wavelengths, and the former line falls in the wavelength coverage of SPICA/SMI-HRS and TMT/MICHI. Here we note that since TMT is a ground-based telescope, the effect of atmospheric absorption has to be considered carefully in selecting lines from the candidate line list. Figure 14 in Appendix C shows the profiles of mid-infrared candidate lines ($\lambda \sim 11 - 25\mu\text{m}$) which trace emission from the hot water vapor within H₂O snowline. All of the lines in this Figure are also listed in Table B.1. Our calculations for a Herbig Ae disk suggest that the fluxes of the stronger candidate H₂O lines in Q band (including 17.75 μm and 24.00 μm lines) are $\sim 10^{-17} - 10^{-18} \text{ W m}^{-2}$. Since HRS on SPICA/SMI has a high sensitivity in Q band, we predict not only successful detections for some Herbig Ae disks, but also suggest the possibility of a survey of the locations of H₂O snowlines in Herbig Ae disks in nearby ($\lesssim 150 \text{ pc}$) star-forming regions for the first time. Moreover, since HRS on SPICA/SMI has an especially high sensitivity,

successful detections are expected even for T Tauri disks in nearby ($\lesssim 150 \text{ pc}$) star-forming regions, as well as Herbig Ae disks in the Orion star-forming region ($\sim 410 \text{ pc}$), with several hours of observations. Our calculations for a T Tauri disk (see Table 1 and B.1) show that the fluxes of the strongest candidate H₂O lines at Q band (including 17.75 μm and 24.00 μm lines) are $\sim 10^{-20} - 10^{-21} \text{ W m}^{-2}$.

We also expect to detect emission from those candidate lines (some of which are not accessible from the ground) which trace emission from the hot water vapor within the H₂O snowline using other high sensitivity mid-infrared and far-infrared instruments on future space telescopes, such as The Mid-Infrared Instrument on board the James Webb Space Telescope (JWST/MIRI⁷), SPICA FAR-infrared Instrument (SPICA/SAFARI), and MRS of SPICA/SMI. Since the spectral resolution of these instruments is not so high (\sim a few thousands), we cannot resolve the velocity profiles of these candidate lines at sufficient resolution to locate the position of the H₂O snowline. However, it will be possible to detect the total fluxes of these candidate lines with these high sensitivity instruments. Our results suggest that these lines mainly trace emission from the hot water vapor within the H₂O snowline. Moreover, since the sensitivity of these instruments is very high, meaning that the time necessary for a detection is not very long, we expect to detect emission from the hot H₂O gas inside the H₂O snowline for various protoplanetary disks, which are suitable candidates for high-dispersion spectroscopic observations with future instruments (e.g., ALMA, SPICA/SMI-HRS).

5. Conclusion

In this paper, we calculated the disk water vapor distribution and corresponding H₂O line profiles for a Herbig Ae disk, and identified candidate water lines which can locate the position of the H₂O snowline across a wide wavelength range from mid-infrared to sub-millimeter.

First we calculated the chemical composition using a self-consistent physical model of a Herbig Ae

⁶http://www.ir.isas.jaxa.jp/SPICA/SPICA_HP/research-en.html

⁷<http://ircamera.as.arizona.edu/MIRI/index.htm>

disk, and investigated the abundance distributions of H₂O gas and ice, and the position of the H₂O snowline. We found that the abundance of H₂O is high (up to 10⁻⁴) in the inner region with higher temperature ($\gtrsim 170\text{K}$) within $\sim 7-8$ au, relatively high ($\sim 10^{-8}$) between 7–8 au and 14 au (= the position of the H₂O snowline, $\sim 120\text{K}$) near the equatorial plane. In addition, it is relatively high ($\sim 10^{-8} - 10^{-7}$) in the hot surface layer and the photodesorbed region of the outer disk, compared to its value ($\sim 10^{-12}$) in the regions outside the H₂O snowline near the equatorial plane. The position of the H₂O snowline in the Herbig Ae disk is further from the central star compared to that in the T Tauri disk, in agreement with previous studies (e.g., Woitke et al. 2009b).

Second, we calculated the H₂O line profiles, and showed that H₂O emission lines with small Einstein A coefficients ($A_{ul} \sim 10^{-3} - 10^{-6} \text{ s}^{-1}$) and relatively high upper state energies ($E_{\text{up}} \sim 1000\text{K}$) are dominated by emission from the region inside the H₂O snowline, and therefore their profiles potentially contain information which can be used to locate the position of the snowline. Since the fluxes of these lines from Herbig Ae disks are larger than those from T Tauri disks, the possibility of a successful detection is expected to increase for a Herbig Ae disk. The wavelengths of those lines which are the best candidates to locate the position of the H₂O snowline range from mid-infrared to sub-millimeter. The values of total fluxes tend to be larger as the wavelengths of the H₂O lines become shorter. This is because the peak wavelength of the Planck function at the gas temperature around the H₂O snowline ($T_g \sim 100 - 200 \text{ K}$) is in the mid-infrared region.

In addition, we investigated the properties of water lines which have been detected by previous spectroscopic observations (e.g., 63.32 μm , 538.29 μm). These lines are less suited to locate the H₂O snowline, because they are not dominated by emission from the region within the H₂O snowline. The properties of near-, and mid-infrared H₂O emission lines which do not trace emission from the hot water vapor within the H₂O snowline are also discussed.

The wavelengths of such candidate lines which

trace emission from the hot water vapor within H₂O snowline overlap with the capabilities of ALMA and future mid-infrared high-dispersion spectrographs (e.g., SPICA/SMI-HRS). The successful detection in a Herbig Ae disk could be achieved with current ALMA capabilities using several lines. Mid-infrared instruments such as HRS on SPICA/SMI would have a high sensitivity in the Q band (e.g., $\sim 16-18\mu\text{m}$), and we predict not only successful detections for some Herbig Ae disks, but also suggest the possibility of a survey of H₂O snowline locations in many Herbig Ae disks in nearby ($\lesssim 150\text{pc}$) star-forming regions for the first time.

We are grateful to Dr. Itsuki Sakon, Dr. Chris Packham, Dr. Hiroshi Shibai, Dr. Takao Nakagawa, Dr. Takashi Onaka, Dr. Satoshi Okuzumi, Dr. Inga Kamp, and Dr. Eiji Akiyama for their useful comments. We would like to thank the referee for comments that improved our paper. The numerical calculations in this study were carried out on SR16000 at Yukawa Institute for Theoretical Physics (YITP) and computer systems at Kwasan and Hida Observatory (KIPS) in Kyoto University, and PC cluster at Center for Computational Astrophysics, National Astronomical Observatory of Japan. This work is supported by JSPS (Japan Society for the Promotion of Science) Grants-in-Aid for Scientific Research (Grant Number; 23103005, 25108004, 25108005, 25400229, 15H03646), by Grants-in-Aid for JSPS fellows (Grant Number; 16J06887), and by the Astrobiology Center Program of National Institutes of Natural Sciences (NINS) (Grant Number; AB281013). S. N. is grateful for the support from the educational program organized by Unit of Synergetic Studies for Space, Kyoto University. C. W. acknowledges support from the Netherlands Organization for Scientific Research (NWO, program number 639.041.335). Astrophysics at Queen's University Belfast is supported by a grant from the STFC.

A. The vertical distributions of normalized cumulative line emissivity

Figure 13 shows the vertical distributions of the normalized cumulative line emissivity at $r = 5$ au (top two panels), $r = 10$ au (middle two panels), and $r = 30$ au (bottom two panels), and of the gas temperature T_g . The left three panels show the distributions for seven H₂O lines at $\lambda = 17.75\mu\text{m}$, $24.00\mu\text{m}$, $61.32\mu\text{m}$, $94.17\mu\text{m}$, $482.99\mu\text{m}$, $682.66\mu\text{m}$, and $933.28\mu\text{m}$, for the Herbig Ae disk. The right three panels show the distributions for seven H₂O lines at $\lambda = 682.66\mu\text{m}$, $63.32\mu\text{m}$, $538.29\mu\text{m}$, $12.40\mu\text{m}$, $12.45\mu\text{m}$, $4.96\mu\text{m}$, and $4.43\mu\text{m}$. for the Herbig Ae disk. We normalize the cumulative emissivity of each line using the values at $z = -\infty$.

The differences in the properties of the line profiles (see also Figures 4, 5, 6, 7, 8, and 9) come from the differences in A_{ul} , E_{up} , and wavelengths among lines. For the lines with similar wavelengths, the emitting regions tend to be in the upper region of the disk as values of A_{ul} of the lines become larger, since the absorption by excited H₂O molecules increases. In addition, in the sub-millimeter lines, the values of normalized cumulative line emissivity are smaller than unity at $z/r \sim 0$. It is because the values of dust opacity at sub-millimeter wavelengths are smaller than those at infrared wavelengths (see also Figures 5, 6, 8, and 9).

B. H₂O line parameters and fluxes

The detailed parameters, such as transitions ($J_{K_a K_c}$), wavelength, frequency, A_{ul} , E_{up} , and total line fluxes of the candidate ortho-H₂O lines which trace emission from the hot water vapor within the H₂O snowline are listed in Table B.1. In Table B.1, we show the values of the total fluxes from both disks around the Herbig Ae star and the T Tauri star. Some of these lines are also listed in Table 1. The line selection method is described in Section 3.2.3.

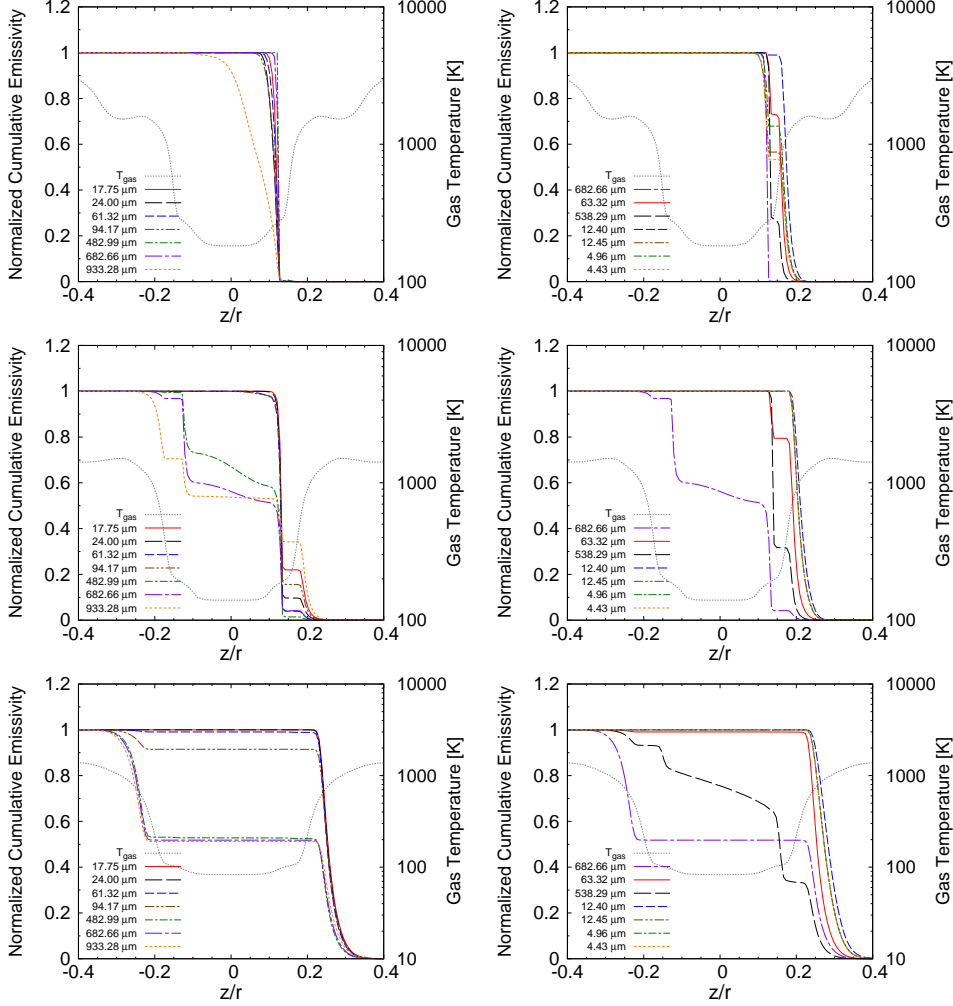


Fig. 13.— The vertical distributions of the normalized cumulative line emissivity at $r = 5$ au (top two panels), $r = 10$ au (middle two panels), and $r = 30$ au (bottom two panels), and of the gas temperature T_g at Kelvin (*gray dotted line*). The left three panels show the distributions for seven pure rotational ortho- H_2O lines at $\lambda = 17.75 \mu\text{m}$ (*red solid line*), $24.00 \mu\text{m}$ (*black long dashed line*), $61.32 \mu\text{m}$ (*blue dashed line*), $94.17 \mu\text{m}$ (*brown dashed two dotted line*), $482.99 \mu\text{m}$ (*green dashed dotted line*), $682.66 \mu\text{m}$ (*violet long dashed dotted line*), and $933.28 \mu\text{m}$ (*orange dotted line*). The right three panels show the distributions for seven pure rotational ortho- H_2O lines at $\lambda = 682.66 \mu\text{m}$ (*violet long dashed dotted line*), $63.32 \mu\text{m}$ (*red solid line*), $538.29 \mu\text{m}$ (*black long dashed line*), $12.40 \mu\text{m}$ (*blue dashed line*), $12.45 \mu\text{m}$ (*brown dashed two dotted line*), $4.96 \mu\text{m}$ (*green dashed dotted line*), and $4.43 \mu\text{m}$ (*orange dotted line*). We normalized the cumulative emissivity of each line using the values at $z = -\infty$. We assume that the inclination angle of the disk i is 0 degree in making these figures.

TABLE B.1

CANDIDATE ORTHO-H₂O LINE PARAMETERS AND TOTAL LINE FLUXES (11–1000 μ M)

$J_{K_a K_c}$	λ^1 [μ m]	Freq. [GHz]	A_{ul} [s ⁻¹]	E_{up} [K]	H Ae flux ^{2,3} [W m ⁻²]	TT flux ^{3,4} [W m ⁻²]
7 ₇₀ -6 ₂₅	11.878	25239.615	6.653×10^{-3}	2006.8	3.4×10^{-19}	1.8×10^{-22}
7 ₆₁ -6 ₁₆	13.005	23052.310	2.585×10^{-4}	1749.8	2.9×10^{-18}	1.1×10^{-21}
6 ₆₁ -5 ₁₄	15.489	19354.618	4.138×10^{-4}	1503.6	6.9×10^{-18}	2.6×10^{-21}
7 ₇₀ -7 ₂₅	16.329	18359.435	7.756×10^{-5}	2006.8	3.8×10^{-19}	1.6×10^{-22}
6 ₆₁ -6 ₁₆	16.728	17921.765	2.153×10^{-5}	1503.6	3.2×10^{-19}	1.1×10^{-22}
6 ₅₂ -5 ₀₅	17.754	16885.840	2.909×10^{-3}	1278.5	4.1×10^{-17}	2.3×10^{-20}
7 ₆₁ -7 ₁₆	19.532	15348.791	1.269×10^{-3}	1749.8	8.3×10^{-18}	3.5×10^{-21}
7 ₇₀ -8 ₂₇	19.638	15265.853	1.900×10^{-6}	2006.8	7.6×10^{-21}	3.1×10^{-24}
7 ₅₂ -7 ₀₇	21.115	14197.932	2.078×10^{-3}	1524.8	2.0×10^{-17}	9.9×10^{-21}
7 ₆₁ -8 ₁₈	21.185	14151.161	6.154×10^{-6}	1749.8	4.8×10^{-20}	1.7×10^{-23}
7 ₇₀ -7 ₄₃	21.571	13897.693	3.474×10^{-3}	2006.8	1.1×10^{-17}	5.5×10^{-21}
5 ₅₀ -5 ₀₅	23.996	12493.205	2.696×10^{-4}	1067.7	9.4×10^{-18}	6.4×10^{-21}
6 ₆₁ -6 ₃₄	25.247	11874.160	3.803×10^{-3}	1503.6	2.6×10^{-17}	1.9×10^{-20}
6 ₆₁ -7 ₁₆	29.339	10218.246	1.859×10^{-5}	1503.6	2.5×10^{-19}	1.3×10^{-22}
8 ₅₄ -9 ₀₉	29.851	10043.001	1.605×10^{-4}	1805.9	1.2×10^{-18}	4.7×10^{-22}
6 ₅₂ -7 ₀₇	33.074	9064.381	5.942×10^{-5}	1278.5	1.4×10^{-18}	1.3×10^{-21}
5 ₅₀ -5 ₂₃	33.833	8860.835	4.552×10^{-3}	1067.7	3.2×10^{-17}	7.1×10^{-20}
7 ₇₀ -8 ₄₅	36.750	8157.523	1.123×10^{-4}	2006.8	4.3×10^{-19}	1.6×10^{-22}
4 ₄₁ -4 ₁₄	37.984	7892.616	2.629×10^{-3}	702.3	3.1×10^{-17}	1.0×10^{-19}
9 ₄₅ -10 ₁₁₀	40.702	7365.464	4.815×10^{-4}	1957.1	2.1×10^{-18}	1.1×10^{-21}
7 ₆₁ -8 ₃₆	47.601	6297.997	4.268×10^{-4}	1749.8	2.3×10^{-18}	2.2×10^{-21}
6 ₆₁ -7 ₃₄	49.334	6076.834	1.195×10^{-4}	1503.6	1.3×10^{-18}	1.8×10^{-21}
5 ₅₀ -6 ₂₅	52.864	5671.021	1.442×10^{-4}	1067.7	3.7×10^{-18}	1.4×10^{-20}
7 ₄₃ -8 ₁₈	53.455	5608.351	5.030×10^{-4}	1339.8	5.2×10^{-18}	1.6×10^{-20}
7 ₅₂ -8 ₂₇	57.394	5223.441	7.203×10^{-4}	1524.8	4.1×10^{-18}	1.1×10^{-20}
5 ₄₁ -6 ₁₆	61.316	4889.280	2.686×10^{-4}	878.1	5.9×10^{-18}	3.5×10^{-20}
6 ₅₂ -7 ₂₅	94.172	3183.464	3.387×10^{-4}	1278.5	1.8×10^{-18}	1.6×10^{-20}
4 ₄₁ -5 ₁₄	112.803	2657.666	1.670×10^{-4}	702.3	1.8×10^{-18}	2.3×10^{-20}
9 ₂₇ -10 ₁₁₀	114.454	2619.334	6.768×10^{-4}	1729.3	1.0×10^{-18}	8.1×10^{-21}
8 ₃₆ -9 ₀₉	116.350	2576.644	7.255×10^{-4}	1447.5	1.4×10^{-18}	1.5×10^{-20}
8 ₄₅ -7 ₅₂	159.051	1884.888	7.403×10^{-3}	1615.3	1.1×10^{-18}	1.7×10^{-20}
6 ₃₄ -7 ₀₇	159.400	1880.753	3.911×10^{-4}	933.7	9.0×10^{-19}	1.5×10^{-20}
8 ₅₄ -9 ₂₇	187.810	1595.252	2.947×10^{-4}	1805.9	2.5×10^{-19}	3.8×10^{-21}
6 ₄₃ -7 ₁₆	190.437	1574.232	2.927×10^{-4}	1088.7	4.9×10^{-19}	8.9×10^{-21}
6 ₂₅ -5 ₃₂	226.761	1322.065	2.334×10^{-3}	795.5	6.0×10^{-19}	1.2×10^{-20}
8 ₄₅ -9 ₁₈	229.206	1307.963	2.599×10^{-4}	1615.3	2.0×10^{-19}	3.9×10^{-21}
8 ₂₇ -7 ₃₄	231.248	1296.411	1.074×10^{-3}	1274.1	3.7×10^{-19}	6.8×10^{-21}
7 ₄₃ -6 ₅₂	234.531	1278.266	1.552×10^{-3}	1399.8	3.6×10^{-19}	6.7×10^{-21}
8 ₅₄ -7 ₆₁	256.593	1168.358	9.459×10^{-4}	1805.9	1.8×10^{-19}	3.5×10^{-21}
6 ₃₄ -5 ₄₁	258.816	1158.324	1.417×10^{-3}	933.7	3.5×10^{-19}	7.0×10^{-21}

TABLE B.1—*Continued*

$J_{K_a K_c}$	λ^1 [μm]	Freq. [GHz]	A_{ul} [s^{-1}]	E_{up} [K]	HAe flux ^{2,3} [W m^{-2}]	TT flux ^{3,4} [W m^{-2}]
7 ₂₅ -8 ₁₈	261.457	1147.621	1.087×10^{-4}	1125.7	1.9×10^{-19}	3.9×10^{-21}
5 ₃₂ -4 ₄₁	482.990	620.701	1.106×10^{-4}	732.1	5.3×10^{-20}	1.1×10^{-21}
7 ₅₂ -6 ₆₁	676.704	443.018	2.231×10^{-5}	1524.8	9.4×10^{-21}	2.6×10^{-22}
6 ₄₃ -5 ₅₀	682.664	439.151	2.816×10^{-5}	1088.7	1.4×10^{-20}	3.1×10^{-22}
10 ₂₉ -9 ₃₆	933.277	321.226	6.165×10^{-6}	1861.2	2.3×10^{-21}	7.8×10^{-23}

¹In calculating the value of line wavelength from the value of line frequency, we use the value of speed of light $c=2.99792458 \times 10^8 \text{ m s}^{-1}$.

²The total flux of each emission line from the Herbig Ae disk.

³In calculating the total fluxes of these H₂O lines, we use a distance $d = 140\text{pc}$ and an inclination angle of $i = 30$ degree.

⁴The total flux of each emission line from the T Tauri disk (see also paper I, Notsu et al. 2016).

C. The profiles of candidate mid-infrared H₂O lines to trace the H₂O snowline

Figure 14 shows the profiles of mid-infrared candidate H₂O lines which trace the hot water vapor within the H₂O snowline ($\lambda \sim 11 - 25\mu\text{m}$). All of the lines in this Figure are also listed in Table B.1. We discuss the properties of these lines in Sections 3.2.3 and 4.4.

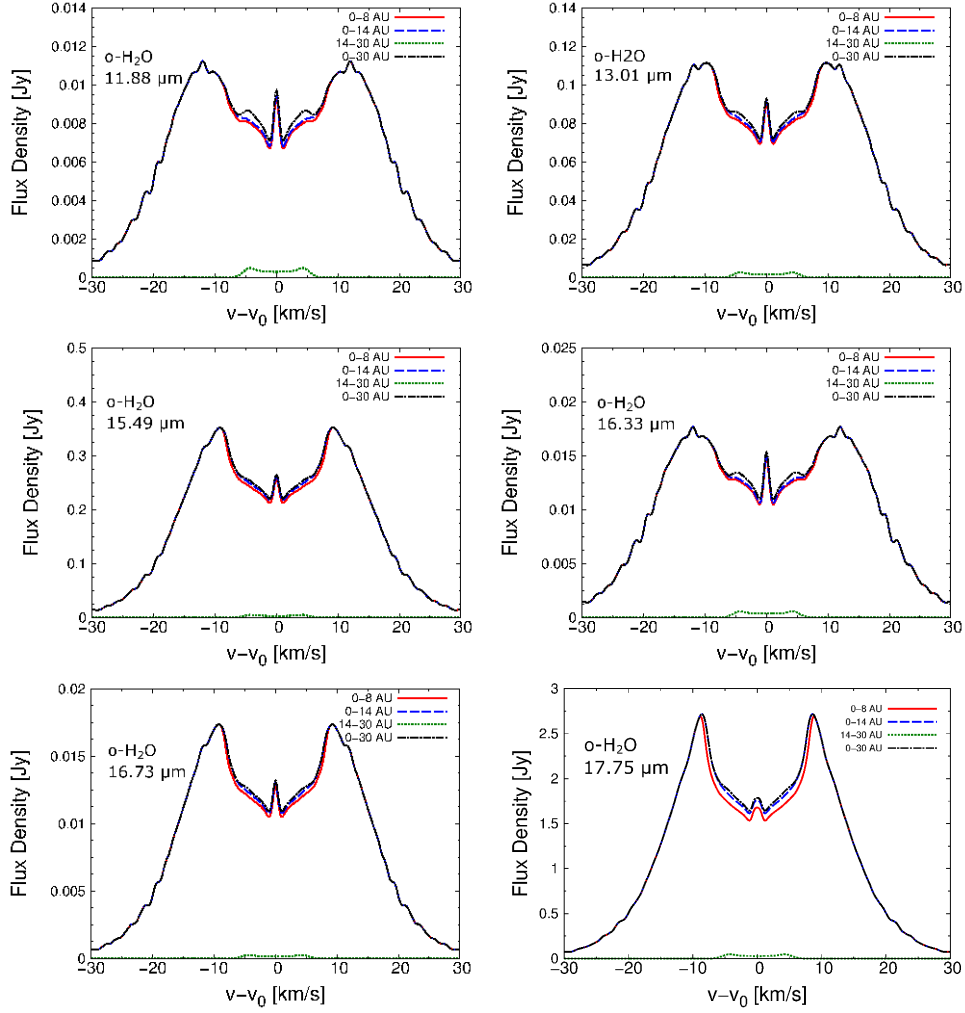


Fig. 14.— The velocity profiles of mid-infrared ortho-H₂O lines at $\lambda=11.88\mu\text{m}$ (top left), $13.01\mu\text{m}$ (top right), $15.49\mu\text{m}$ (middle left), $16.33\mu\text{m}$ (middle right), $16.73\mu\text{m}$ (bottom left), and $17.75\mu\text{m}$ (bottom right), from the Herbig Ae disk. These exist between $11\text{-}25\mu\text{m}$ and are also the best mid-infrared candidate ortho-H₂O lines to trace the hot water vapor within the H₂O snowline. The parameters and total fluxes of these ortho-H₂O lines are reported in Table B.1. *Red solid lines* are the emission line profiles from inside 8 au (=the inner high temperature region), *blue dashed lines* are those from inside 14 au (\sim inside the H₂O snowline), *green dotted lines* are those from 14-30 au (\sim outside the H₂O snowline), and *black dashed dotted lines* are those from the total area inside 30au.

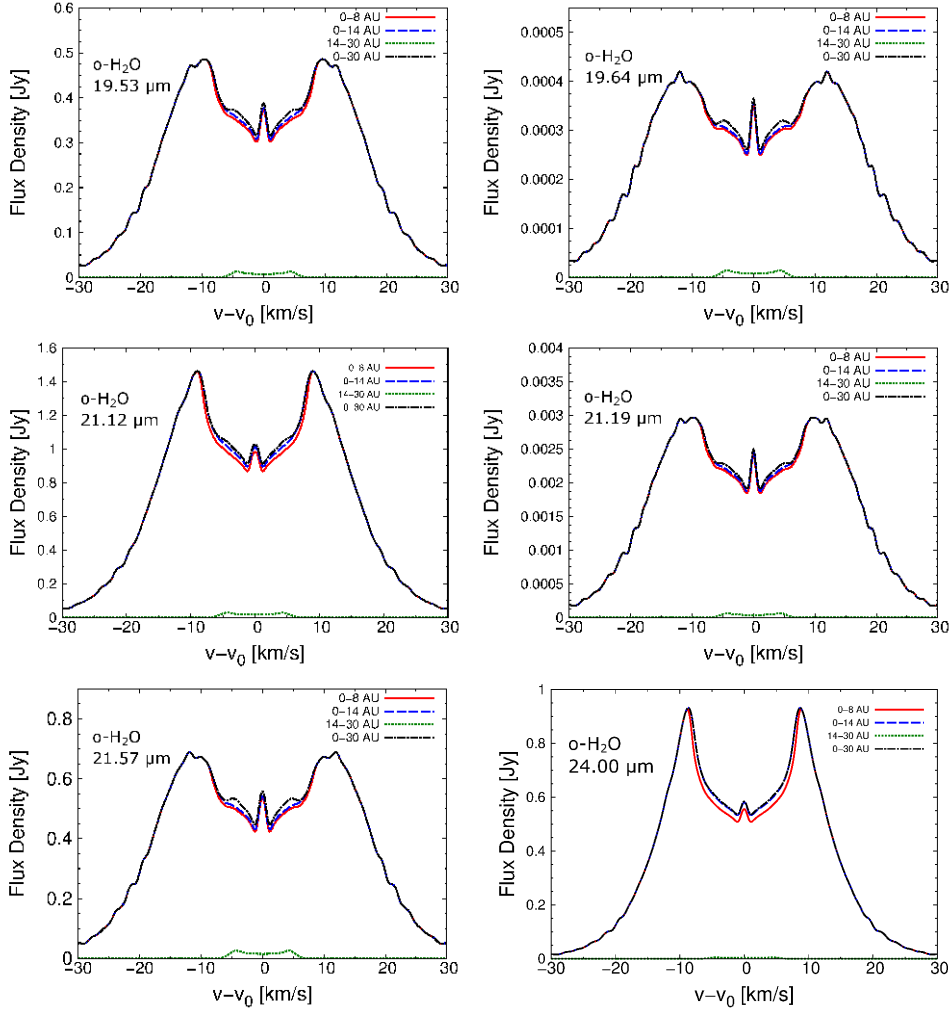


Fig. 14.— (Continued.) The velocity profiles of mid-infrared ortho-H₂O lines at $\lambda=19.53\mu\text{m}$ (top left), $19.64\mu\text{m}$ (top right), $21.12\mu\text{m}$ (middle left), $21.19\mu\text{m}$ (middle right), $21.57\mu\text{m}$ (bottom left), and $24.00\mu\text{m}$ (bottom right), from the Herbig Ae disk.

REFERENCES

- Aikawa, Y., & Nomura, H. 2006, *ApJ*, 642, 1152
- Akimkin, V., Zhukovska, S., Wiebe, D., et al. 2013, *ApJ*, 766, 8
- ALMA Partnership, Brogan, C. L., Pérez, L. M., et al. 2015, *ApJ*, 808, L3
- Andrews, S. M., Wilner, D. J., Zhu, Z., et al. 2016, *ApJ*, 820, L40
- Antonellini, S., Kamp, I., Lahuis, F., et al. 2016, *A&A*, 585, A61
- Antonellini, S., Kamp, I., Riviere-Marichalar, P., et al. 2015, *A&A*, 582, A105
- Banzatti, A., Meyer, M. R., Bruderer, S., et al. 2012, *ApJ*, 745, 90
- Banzatti, A., Pinilla, P., Ricci, L., et al. 2015, *ApJ*, 815, L15
- Banzatti, A., Pontoppidan, K. M., Salyk, C., et al. 2016, *ApJ* in press, arXiv:1611.06230
- Benisty, M., Tatulli, E., Ménard, F., & Swain, M. R. 2010, *A&A*, 511, A75
- Bethell, T. J., & Bergin, E. A. 2011, *ApJ*, 739, 78
- Blevins, S. M., Pontoppidan, K. M., Banzatti, A., et al. 2016, *ApJ*, 818, 22
- Cieza, L. A., Casassus, S., Tobin, J., et al. 2016, *Nature*, 535, 258
- Davis, S. S. 2005, *ApJ*, 620, 994
- Dent, W. R. F., Thi, W. F., Kamp, I., et al. 2013, *PASP*, 125, 477
- Dominik, C., Dullemond, C. P., Waters, L. B. F. M., & Walch, S. 2003, *A&A*, 398, 607
- Du, F., & Bergin, E. A. 2014, *ApJ*, 792, 2
- Dullemond, C. P., & Dominik, C. 2004, *A&A*, 417, 159
- Dutrey, A., Semenov, D., Chapillon, E., et al. 2014, *Protostars and Planets VI*, University of Arizona Press, 317
- Espaillet, C., Calvet, N., D'Alessio, P., et al. 2007, *ApJ*, 670, L135
- Eistrup, C., Walsh, C., & van Dishoeck, E. F. 2016, *A&A*, 595, A83
- Faure, A., & Josselin, E. 2008, *A&A*, 492, 257
- Fedele, D., Bruderer, S., van Dishoeck, E. F., et al. 2012, *A&A*, 544, LL9
- Fedele, D., Bruderer, S., van Dishoeck, E. F., et al. 2013, *A&A*, 559, AA77
- Fedele, D., Pascucci, I., Brittain, S., et al. 2011, *ApJ*, 732, 106
- Fujiwara, H., Honda, M., Kataza, H., et al. 2006, *ApJ*, 644, L133
- Fukagawa, M., Tamura, M., Itoh, Y., et al. 2006, *ApJ*, 636, L153
- Fukagawa, M., Tsukagoshi, T., Momose, M., et al. 2013, *PASJ*, 65, L14
- Furuya, K., Aikawa, Y., Nomura, H., Hersant, F., & Wakelam, V. 2013, *ApJ*, 779, 11
- Garaud, P., & Lin, D. N. C. 2007, *ApJ*, 654, 606
- Graedel, T. E., Langer, W. D., & Frerking, M. A. 1982, *ApJS*, 48, 321
- Harsono, D., Bruderer, S., & van Dishoeck, E. F. 2015, *A&A*, 582, A41
- Hasegawa, T. I., Herbst, E., & Leung, C. M. 1992, *ApJS*, 82, 167
- Haworth, T. J., Ilee, J. D., Forgan, D. H., et al. 2016, *PASA*, 33, e053
- Hayashi, C. 1981, *Progress of Theoretical Physics Supplement*, 70, 35
- Hayashi, C., Nakazawa, K., & Nakagawa, Y. 1985, *Protostars and Planets II*, University of Arizona Press, 1100
- Heinzeller, D., Nomura, H., Walsh, C., & Millar, T. J. 2011, *ApJ*, 731, 115
- Henning, T., & Semenov, D. 2013, *Chemical Reviews*, 113, 9016
- Hirota, T., Kim, M. K., Kuroono, Y., & Honma, M. 2014, *ApJ*, 782, L28
- Hogerheijde, M. R., Bergin, E. A., Brinch, C., et al. 2011, *Science*, 334, 338

- Hogerheijde, M. R., & van der Tak, F. F. S. 2000, *A&A*, 362, 697
- Honda, M., Maaskant, K., Okamoto, Y. K., et al. 2012, *ApJ*, 752, 143
- Honda, M., Maaskant, K., Okamoto, Y. K., et al. 2015, *ApJ*, 804, 143
- Isella, A., Guidi, G., Testi, L., et al. 2016, *Phys. Rev. Lett.* 117, 251101
- Kamp, I., Thi, W.-F., Meeus, G., et al. 2013, *A&A*, 559, A24
- Kenyon, S. J., & Hartmann, L. 1995, *ApJS*, 101, 117
- Krijt, S., Ciesla, F. J., & Bergin, E. A. 2016, *ApJ* in press, arXiv:1610.06463
- Kristensen, L. E., Brown, J. M., Wilner, D., & Salyk, C. 2016, *ApJ*, 822, L20
- Lahuis, F., van Dishoeck, E. F., Blake, G. A., et al. 2007, *ApJ*, 665, 492
- Maaskant, K. M., Honda, M., Waters, L. B. F. M., et al. 2013, *A&A*, 555, A64
- Mandell, A. M., Bast, J., van Dishoeck, E. F., et al. 2012, *ApJ*, 747, 92
- Mathis, J. S., Rumpl, W., & Nordsieck, K. H. 1977, *ApJ*, 217, 425
- Meeus, G., Montesinos, B., Mendigutía, I., et al. 2012, *A&A*, 544, AA78
- Meeus, G., Waters, L. B. F. M., Bouwman, J., et al. 2001, *A&A*, 365, 476
- Meijerink, R., Poelman, D. R., Spaans, M., Tielens, A. G. G. M., & Glassgold, A. E. 2008, *ApJ*, 689, L57
- Meijerink, R., Pontoppidan, K. M., Blake, G. A., Poelman, D. R., & Dullemond, C. P. 2009, *ApJ*, 704, 1471
- Menu, J., van Boekel, R., Henning, T., et al. 2015, *A&A*, 581, A107
- Min, M., Bouwman, J., Dominik, C., et al. 2016, *A&A*, 593, A11
- Min, M., Dullemond, C. P., Kama, M., & Dominik, C. 2011, *Icarus*, 212, 416
- Morbidelli, A., Bitsch, B., Crida, A., et al. 2016, *Icarus*, 267, 368
- Morbidelli, A., Chambers, J., Lunine, J. I., et al. 2000, *Meteoritics and Planetary Science*, 35, 1309
- Morbidelli, A., Lunine, J. I., O'Brien, D. P., Raymond, S. N., & Walsh, K. J. 2012, *Annual Review of Earth and Planetary Sciences*, 40, 251
- Mulders, G. D., Ciesla, F. J., Min, M., & Pascucci, I. 2015, *ApJ*, 807, 9
- Nomura, H., & Millar, T. J. 2005, *A&A*, 438, 923
- Nomura, H., Aikawa, Y., Tsujimoto, M., Nakagawa, Y., & Millar, T. J. 2007, *ApJ*, 661, 334
- Notsu, S., Nomura, H., Ishimoto, D., Walsh, C., Honda, M., Hirota, T., & Millar, T. J. 2016, *ApJ*, 827, 113
- Notsu, S., Nomura, H., Ishimoto, D., et al. 2015, *Revolution in Astronomy with ALMA: The Third Year*, ASP Conference Series, 499, 289
- Öberg, K. I., Murray-Clay, R., & Bergin, E. A. 2011, *ApJ*, 743, L16
- Oka, A., Nakamoto, T., & Ida, S. 2011, *ApJ*, 738, 141
- Okuzumi, S., Momose, M., Sirono, S.-i., Kobayashi, H., & Tanaka, H. 2016, *ApJ*, 821, 82
- Okuzumi, S., Tanaka, H., Kobayashi, H., & Wada, K. 2012, *ApJ*, 752, 106
- Packham, C., Honda, M., Richter, M., et al. 2012, *Proc. SPIE*, 8446, 84467G
- Panić, O., Ratzka, T., Mulders, G. D., et al. 2014, *A&A*, 562, A101
- Piso, A.-M. A., Öberg, K. I., Birnstiel, T., & Murray-Clay, R. A. 2015, *ApJ*, 815, 109
- Podio, L., Kamp, I., Codella, C., et al. 2013, *ApJ*, 766, L5
- Pontoppidan, K. M., Salyk, C., Blake, G. A., et al. 2010a, *ApJ*, 720, 887

- Pontoppidan, K. M., Salyk, C., Blake, G. A., & Küstner, H. U. 2010b, *ApJ*, 722, L173
- Ros, K., & Johansen, A. 2013, *A&A*, 552, A137
- Rybicki, G. B., & Lightman, A. P. 1986, *Radiative Processes in Astrophysics*, by George B. Rybicki, Alan P. Lightman, pp. 400. ISBN 0-471-82759-2. Wiley-VCH, June 1986
- Salinas, V. N., Hogerheijde, M. R., Bergin, E. A., et al. 2016, *A&A*, 591, A122
- Salyk, C., Pontoppidan, K. M., Blake, G. A., et al. 2008, *ApJ*, 676, L49
- Salyk, C., Pontoppidan, K. M., Blake, G. A., Najita, J. R., & Carr, J. S. 2011, *ApJ*, 731, 130
- Sato, T., Okuzumi, S., & Ida, S. 2016, *A&A*, 589, A15
- Schöier, F. L., van der Tak, F. F. S., van Dishoeck, E. F., & Black, J. H. 2005, *A&A*, 432, 369
- Strom, K. M., Strom, S. E., Edwards, S., Cabrit, S., & Skrutskie, M. F. 1989, *AJ*, 97, 1451
- Tilling, I., Woitke, P., Meeus, G., et al. 2012, *A&A*, 538, A20
- Tsukagoshi, T., Nomura, H., Muto, T., et al. 2016, *ApJ*, 829, L35
- van Dishoeck, E. F., Bergin, E. A., Lis, D. C., & Lunine, J. I. 2014, *Protostars and Planets VI*, University of Arizona Press, 835
- Vasyunin, A. I., Wiebe, D. S., Birnstiel, T., et al. 2011, *ApJ*, 727, 76
- Wada, K., Tanaka, H., Okuzumi, S., et al. 2013, *A&A*, 559, AA62
- Walsh, C., Juhász, A., Pinilla, P., et al. 2014b, *ApJ*, 791, L6
- Walsh, C., Millar, T. J., & Nomura, H. 2010, *ApJ*, 722, 1607
- Walsh, C., Millar, T. J., Nomura, H., et al. 2014a, *A&A*, 563, AA33
- Walsh, C., Nomura, H., Millar, T. J., & Aikawa, Y. 2012, *ApJ*, 747, 114
- Walsh, C., Nomura, H., & van Dishoeck, E. 2015, *A&A*, 582, A88
- Weingartner, J. C., & Draine, B. T. 2001, *ApJ*, 548, 296
- Woitke, P., Thi, W.-F., Kamp, I., & Hogerheijde, M. R. 2009b, *A&A*, 501, L5
- Woodall, J., Agúndez, M., Markwick-Kemper, A. J., & Millar, T. J. 2007, *A&A*, 466, 1197
- Zhang, K., Bergin, E. A., Blake, G. A., et al. 2016, *ApJ*, 818, L16
- Zhang, K., Blake, G. A., & Bergin, E. A. 2015, *ApJ*, 806, L7
- Zhang, K., Pontoppidan, K. M., Salyk, C., & Blake, G. A. 2013, *ApJ*, 766, 82